

1 Constraining the High-Energy Emission from Gamma-ray Bursts 2 with *Fermi*

3 The *Fermi* Large Area Telescope Team

4 M. Ackermann¹, M. Ajello², L. Baldini³, G. Barbiellini^{4,5}, M. G. Baring⁶, K. Bechtol²,
5 R. Bellazzini³, R. D. Blandford², E. D. Bloom², E. Bonamente^{8,9}, A. W. Borgland²,
6 E. Bottacini², A. Bouvier¹⁰, M. Brigida^{11,12}, R. Buehler², S. Buson^{14,15}, G. A. Caliandro¹⁶,
7 R. A. Cameron², C. Cecchi^{8,9}, E. Charles², A. Chekhtman¹⁷, J. Chiang^{2,18}, S. Ciprini^{19,9},
8 R. Claus², J. Cohen-Tanugi²⁰, V. Connaughton^{13,21}, S. Cutini²², F. D'Ammando^{23,24},
9 F. de Palma^{11,12}, C. D. Dermer²⁵, E. do Couto e Silva², P. S. Drell², A. Drlica-Wagner²,
10 C. Favuzzi^{11,12}, Y. Fukazawa²⁷, P. Fusco^{11,12}, F. Gargano¹², D. Gasparrini²², N. Gehrels²⁸,
11 S. Germani^{8,9}, N. Giglietto^{11,12}, F. Giordano^{11,12}, M. Giroletti²⁹, T. Glanzman²,
12 J. Granot³⁰, I. A. Grenier³¹, J. E. Grove²⁵, S. Guiriec¹³, D. Hadasch¹⁶, Y. Hanabata²⁷,
13 A. K. Harding²⁸, E. Hays²⁸, D. Horan³³, G. Jóhannesson³⁴, J. Kataoka³⁵,
14 J. Knödseder^{36,37}, D. Kocevski^{2,38}, M. Kuss³, J. Lande², F. Longo^{4,5}, F. Loparco^{11,12},
15 M. N. Lovellette²⁵, P. Lubrano^{8,9}, M. N. Mazziotta¹², S. McGlynn³⁹, P. F. Michelson²,
16 W. Mitthumsiri², M. E. Monzani², E. Moretti^{40,41,42}, A. Morselli⁴³, I. V. Moskalenko²,
17 S. Murgia², M. Naumann-Godo³¹, J. P. Norris⁴⁴, E. Nuss²⁰, T. Nymark^{40,41}, T. Ohsugi⁴⁵,
18 A. Okumura^{2,46}, N. Omodei², E. Orlando^{2,32}, J. H. Panetta², D. Parent⁴⁷, V. Pelassa¹³,
19 M. Pesce-Rollins³, F. Piron²⁰, G. Pivato¹⁵, J. L. Racusin²⁸, S. Rainò^{11,12}, R. Rando^{14,15},
20 S. Razzaque⁴⁷, A. Reimer^{7,2}, O. Reimer^{7,2}, S. Ritz¹⁰, F. Ryde^{40,41}, C. Sgrò³, E. J. Siskind⁴⁸,
21 E. Sonbas^{28,49,50}, G. Spandre³, P. Spinelli^{11,12}, M. Stamatikos^{28,51}, Lukasz Stawarz^{46,52},
22 D. J. Suson⁵³, H. Takahashi⁴⁵, T. Tanaka², J. G. Thayer², J. B. Thayer², L. Tibaldo^{14,15},
23 M. Tinivella³, G. Tosti^{8,9}, T. Uehara²⁷, J. Vandenbroucke², V. Vasileiou²⁰, G. Vianello^{2,54},
24 V. Vitale^{43,55}, A. P. Waite²

25 The *Fermi* Gamma-ray Burst Monitor Team

26 V. Connaughton¹³, M. S. Briggs^{13,56}, S. Guirec²⁸, A. Goldstein¹³, J. M. Burgess¹³,
27 P. N. Bhat¹³, E. Bissaldi⁷, A. Camero-Arranz (50,58) J. Fishman¹³, G. Fitzpatrick²⁶,
28 S. Foley^{26,32}, D. Gruber³², P. Jenke⁵⁸, R. M. Kippen⁵⁷, C. Kouveliotou⁵⁸, S. McBreen^{26,32},
29 C. Meegan⁵⁰, W. S. Paciesas¹³, R. Preece¹³, A. Rau³², D. Tierney²⁶,
30 A. J. van der Horst^{58,59}, A. von Kienlin³², C. Wilson-Hodge⁵⁸, S. Xiong¹³

¹Deutsches Elektronen Synchrotron DESY, D-15738 Zeuthen, Germany

²W. W. Hansen Experimental Physics Laboratory, Kavli Institute for Particle Astrophysics and Cosmology, Department of Physics and SLAC National Accelerator Laboratory, Stanford University, Stanford, CA 94305, USA

³Istituto Nazionale di Fisica Nucleare, Sezione di Pisa, I-56127 Pisa, Italy

⁴Istituto Nazionale di Fisica Nucleare, Sezione di Trieste, I-34127 Trieste, Italy

⁵Dipartimento di Fisica, Università di Trieste, I-34127 Trieste, Italy

⁶Rice University, Department of Physics and Astronomy, MS-108, P. O. Box 1892, Houston, TX 77251, USA

⁷Institut für Astro- und Teilchenphysik and Institut für Theoretische Physik, Leopold-Franzens-Universität Innsbruck, A-6020 Innsbruck, Austria

⁸Istituto Nazionale di Fisica Nucleare, Sezione di Perugia, I-06123 Perugia, Italy

⁹Dipartimento di Fisica, Università degli Studi di Perugia, I-06123 Perugia, Italy

¹⁰Santa Cruz Institute for Particle Physics, Department of Physics and Department of Astronomy and Astrophysics, University of California at Santa Cruz, Santa Cruz, CA 95064, USA

¹¹Dipartimento di Fisica “M. Merlin” dell’Università e del Politecnico di Bari, I-70126 Bari, Italy

¹²Istituto Nazionale di Fisica Nucleare, Sezione di Bari, 70126 Bari, Italy

¹³Center for Space Plasma and Aeronomic Research (CSPAR), University of Alabama in Huntsville, Huntsville, AL 35899, USA

¹⁴Istituto Nazionale di Fisica Nucleare, Sezione di Padova, I-35131 Padova, Italy

¹⁵Dipartimento di Fisica “G. Galilei”, Università di Padova, I-35131 Padova, Italy

¹⁶Institut de Ciències de l’Espai (IEEE-CSIC), Campus UAB, 08193 Barcelona, Spain

¹⁷Artep Inc., 2922 Excelsior Springs Court, Ellicott City, MD 21042, resident at Naval Research Laboratory, Washington, DC 20375, USA

¹⁸email: jchiang@slac.stanford.edu

¹⁹ASI Science Data Center, I-00044 Frascati (Roma), Italy

²⁰Laboratoire Univers et Particules de Montpellier, Université Montpellier 2, CNRS/IN2P3, Montpellier, France

²¹email: connav@uah.edu

²²Agenzia Spaziale Italiana (ASI) Science Data Center, I-00044 Frascati (Roma), Italy

²³IASF Palermo, 90146 Palermo, Italy

²⁴INAF-Istituto di Astrofisica Spaziale e Fisica Cosmica, I-00133 Roma, Italy

²⁵Space Science Division, Naval Research Laboratory, Washington, DC 20375-5352, USA

-
- ²⁶University College Dublin, Belfield, Dublin 4, Ireland
- ²⁷Department of Physical Sciences, Hiroshima University, Higashi-Hiroshima, Hiroshima 739-8526, Japan
- ²⁸NASA Goddard Space Flight Center, Greenbelt, MD 20771, USA
- ²⁹INAF Istituto di Radioastronomia, 40129 Bologna, Italy
- ³⁰Centre for Astrophysics Research, Science and Technology Research Institute, University of Hertfordshire, Hatfield AL10 9AB, UK
- ³¹Laboratoire AIM, CEA-IRFU/CNRS/Université Paris Diderot, Service d’Astrophysique, CEA Saclay, 91191 Gif sur Yvette, France
- ³²Max-Planck Institut für extraterrestrische Physik, 85748 Garching, Germany
- ³³Laboratoire Leprince-Ringuet, École polytechnique, CNRS/IN2P3, Palaiseau, France
- ³⁴Science Institute, University of Iceland, IS-107 Reykjavik, Iceland
- ³⁵Research Institute for Science and Engineering, Waseda University, 3-4-1, Okubo, Shinjuku, Tokyo 169-8555, Japan
- ³⁶CNRS, IRAP, F-31028 Toulouse cedex 4, France
- ³⁷GAHEC, Université de Toulouse, UPS-OMP, IRAP, Toulouse, France
- ³⁸email: kocevski@stanford.edu
- ³⁹Exzellenzcluster Universe, Technische Universität München, D-85748 Garching, Germany
- ⁴⁰Department of Physics, Royal Institute of Technology (KTH), AlbaNova, SE-106 91 Stockholm, Sweden
- ⁴¹The Oskar Klein Centre for Cosmoparticle Physics, AlbaNova, SE-106 91 Stockholm, Sweden
- ⁴²email: moretti@particle.kth.se
- ⁴³Istituto Nazionale di Fisica Nucleare, Sezione di Roma “Tor Vergata”, I-00133 Roma, Italy
- ⁴⁴Department of Physics, Boise State University, Boise, ID 83725, USA
- ⁴⁵Hiroshima Astrophysical Science Center, Hiroshima University, Higashi-Hiroshima, Hiroshima 739-8526, Japan
- ⁴⁶Institute of Space and Astronautical Science, JAXA, 3-1-1 Yoshinodai, Chuo-ku, Sagamihara, Kanagawa 252-5210, Japan
- ⁴⁷Center for Earth Observing and Space Research, College of Science, George Mason University, Fairfax, VA 22030, resident at Naval Research Laboratory, Washington, DC 20375, USA
- ⁴⁸NYCB Real-Time Computing Inc., Lattingtown, NY 11560-1025, USA
- ⁴⁹Adıyaman University, 02040 Adıyaman, Turkey
- ⁵⁰Universities Space Research Association (USRA), Columbia, MD 21044, USA
- ⁵¹Department of Physics, Center for Cosmology and Astro-Particle Physics, The Ohio State University,

ABSTRACT

31

32

We examine 288 GRBs detected by the *Fermi* Gamma-ray Space Telescope’s Gamma-ray Burst Monitor (GBM) that fell within the field-of-view of *Fermi*’s Large Area Telescope (LAT) during the first 2.5 years of observations, which showed no evidence for emission above 100 MeV. We report the photon flux upper limits in the 0.1–10 GeV range during the prompt emission phase as well as for fixed 30 s and 100 s integrations starting from the trigger time for each burst. We compare these limits with the fluxes that would be expected from extrapolations of spectral fits presented in the first GBM spectral catalog and infer that roughly half of the GBM-detected bursts either require spectral breaks between the GBM and LAT energy bands or have intrinsically steeper spectra above the peak of the νF_ν spectra (E_{pk}). In order to distinguish between these two scenarios, we perform joint GBM and LAT spectral fits to the 30 brightest GBM-detected bursts and find that a majority of these bursts are indeed softer above E_{pk} than would be inferred from fitting the GBM data alone. Approximately 20% of this spectroscopic subsample show statistically significant evidence for a cut-off in their high-energy spectra, which if assumed to be due to $\gamma\gamma$ attenuation, places limits on the maximum Lorentz factor associated with the relativistic outflow producing this emission. All of these latter bursts have maximum Lorentz factor estimates that are well below the minimum Lorentz factors calculated for LAT-detected GRBs, revealing a wide distribution in the bulk Lorentz factor of GRB outflows and indicating that LAT-detected bursts may represent the high end of this distribution.

Columbus, OH 43210, USA

⁵²Astronomical Observatory, Jagiellonian University, 30-244 Kraków, Poland

⁵³Department of Chemistry and Physics, Purdue University Calumet, Hammond, IN 46323-2094, USA

⁵⁴Consorzio Interuniversitario per la Fisica Spaziale (CIFS), I-10133 Torino, Italy

⁵⁵Dipartimento di Fisica, Università di Roma “Tor Vergata”, I-00133 Roma, Italy

⁵⁶email: michael.briggs@nasa.gov

⁵⁷Los Alamos National Laboratory, Los Alamos, NM 87545, USA

⁵⁸NASA Marshall Space Flight Center, Huntsville, AL 35812, USA

⁵⁹NASA Postdoctoral Program Fellow, USA

⁶⁰email: valerie@nasa.gov

33 *Subject headings:* Gamma-rays: Bursts: Prompt

34 1. Introduction

35 Observations by the *Fermi* Gamma-ray Space Telescope have dramatically increased our
 36 knowledge of the broad-band spectra of gamma-ray bursts (GRBs). The Gamma-ray Burst
 37 Monitor (GBM) on board *Fermi* has detected over 700 GRBs in roughly 3 years of triggered
 38 operations. Of these bursts, 29 have been detected at energies > 100 MeV by *Fermi*'s Large
 39 Area Telescope (LAT); and five of these bursts: GRB 080916C, GRB 090510, GRB 090328,
 40 GRB 090902B, and GRB 090926A, have been detected at energies > 10 GeV. The high-
 41 energy emission from the majority of these bursts show evidence for being consistent with
 42 the high-energy component of the smoothly joined broken power-law, commonly referred to
 43 as the Band spectrum (Band et al. 1993), that has been observed in the GBM energy range.
 44 Three of these bursts: GRB 090510 (Ackermann et al. 2010a), GRB 090902B (Abdo et al.
 45 2009a), and GRB 090926A (Ackermann et al. 2011a), though, exhibit an additional hard
 46 spectral component that is distinct from the continuum emission observed at sub-MeV en-
 47 ergies.

48 Similar high-energy emission above 100 MeV was detected by the Energetic Gamma-Ray
 49 Experiment Telescope (*EGRET*) onboard the Compton Gamma-Ray Observatory and by the
 50 *AGILE* spacecraft (Del Monte et al. 2011). The prompt high-energy emission detected by
 51 *EGRET* from GRB 930131 (Kouveliotou et al. 1994; Sommer et al. 1994) and GRB 940217
 52 (Hurley et al. 1994), was consistent with an extrapolation of the GRB spectrum as measured
 53 by the Burst And Transient Source Experiment (BATSE) in the 25 keV–2 MeV energy range.
 54 *EGRET* observations of GRB 941017 (González et al. 2003), on the other hand, showed
 55 evidence for an additional hard spectral component that extended up to 200 MeV, the first
 56 such detection in a GRB spectrum.

57 Unlike these previous detections by *EGRET*, many of the LAT detected bursts have mea-
 58 sured redshifts, made possible through X-ray localizations by the *Swift* spacecraft (Gehrels et al.
 59 2004) and ground-based follow-up observations of their long-lived afterglow emission. The
 60 high-energy detections, combined with the redshift to these GRBs, have shed new light into
 61 the underlying physics of this emission. At a redshift of $z = 0.903$ (McBreen et al. 2010),
 62 the detection of GeV photons from GRB 090510 indicates a minimum bulk Lorentz factor
 63 of $\Gamma_{\gamma,\min} \sim 1200$ in order for the observed gamma rays to have avoided attenuation due to
 64 electron-positron pair production (Ackermann et al. 2010b). Furthermore, a spectral cut-off

65 at ~ 1.4 GeV is quite evident in the high-energy component of GRB 090926A, which if
 66 interpreted as opacity due to $\gamma\gamma$ attenuation within the emitting region, allows for a direct
 67 estimate of the bulk Lorentz factor of $\Gamma \sim 200\text{--}700$ for the outflow producing the emission
 68 (Ackermann et al. 2011b).

69 Perhaps equally important for unraveling the nature of the prompt emission is the lack
 70 of a significant detection above 100 MeV for the majority of the GRBs detected by the
 71 GBM. The LAT instrument has detected roughly 8% of the GBM-triggered GRBs that
 72 have occurred within the LAT field-of-view (FOV). This detection rate places limits on
 73 the ubiquity of the extra high-energy components detected by LAT, *EGRET*, and *AGILE*.
 74 Such a component would be a natural consequence of synchrotron emission from relativistic
 75 electrons in an internal shock scenario, but, for example, might be suppressed in Poynting
 76 flux dominated models (e.g., see Fan & Piran (2008)). Therefore, a systematic analysis of
 77 the non-detections of high-energy components in GBM-detected GRBs may significantly
 78 help to discriminate between various prompt emission mechanisms. Furthermore, the lack
 79 of a detection by the LAT of GBM-detected GRBs with particularly hard spectra points to
 80 intrinsic spectral cut-offs and/or curvature at high energies, giving us further insight into
 81 the physical properties of the emitting region.

82 In this paper, we examine the GBM-detected bursts that fell within the LAT field-of-
 83 view at the time of trigger during the first 2.5 years of observations which showed no evidence
 84 for emission above 100 MeV. We report the photon flux upper limits in the 0.1–10 GeV
 85 band during the prompt emission phase and for 30 s and 100 s integrations starting from the
 86 trigger time for each burst. We then compare these upper limits with the fluxes that would
 87 be expected from extrapolations of spectral fits presented in the first GBM spectral catalog
 88 (Goldstein et al., in press) in order to determine how well measurements of the \lesssim MeV
 89 properties of GRBs can predict detections at > 100 MeV energies.

90 We find that roughly half of the GBM detected bursts either require spectral breaks or
 91 have intrinsically steeper spectra in order to explain their non-detections by the LAT. We
 92 distinguish between these two scenarios by performing joint GBM and LAT spectral fits to a
 93 subset of the 30 brightest bursts, as seen by the GBM that were simultaneously in the LAT
 94 field of view. We find that while a majority of these bursts have spectra that are softer above
 95 the peak of the νF_ν spectra (E_{pk}) than would be inferred from fitting the GBM data alone,
 96 a subset of bright bursts have a statistically significant high-energy spectral cut-off similar
 97 to the spectral break reported for GRB 090926A (Ackermann et al. 2011b). Finally, we use
 98 our joint GBM and LAT spectral fits in conjunction with the LAT non-detections at 100
 99 MeV to place limits on the maximum Lorentz factor for these GRBs which show evidence
 100 for intrinsic spectral breaks

101 The paper is structured as follows: In section 2, we review the characteristics of the
102 GBM and LAT instruments, and in section 3, we define the GRB samples considered in this
103 work. In section 4, we describe the analysis we perform to quantify the significance of the
104 LAT non-detections; we present the results in section 5, and discuss the implications they
105 have on our understanding of the properties associated with the prompt gamma-ray emission
106 in section 6.

107 2. The LAT and GBM Instruments

108 The *Fermi* Gamma-ray Space Telescope carries the Gamma-ray Burst Monitor (Meegan et al.
109 2009a) and the Large Area Telescope (Atwood et al. 2009). The GBM has 14 scintillation
110 detectors that together view the entire unocculted sky. Triggering and localization are per-
111 formed using 12 sodium iodide (NaI) and 2 bismuth germanate (BGO) detectors with dif-
112 ferent orientations placed around the spacecraft. The two BGO scintillators are placed on
113 opposite sides of the spacecraft so that at least one detector is in view for any direction on
114 the sky. GBM spectroscopy uses both the NaI and BGO detectors, sensitive between 8 keV
115 and 1 MeV, and 150 keV and 40 MeV, respectively, so that their combination provides an
116 unprecedented 4 decades of energy coverage with which to perform spectroscopic studies of
117 GRBs.

118 The LAT is a pair conversion telescope comprising a 4×4 array of silicon strip track-
119 ers and cesium iodide (CsI) calorimeters covered by a segmented anti-coincidence detector
120 (ACD) to reject charged-particle background events. The LAT covers the energy range from
121 20 MeV to more than 300 GeV with a field-of-view of ~ 2.4 steradians. The dead time per
122 event of the LAT is nominally $26.50 \mu\text{s}$ for most events, although about 10% of the event
123 read outs include more calibration data, which engender longer dead times. This dead time
124 is 4 orders of magnitude shorter than that of *EGRET*. This is crucial for observations of
125 high-intensity transient events such as GRBs. The LAT triggers on many more background
126 events than celestial gamma rays. Onboard background rejection is supplemented on the
127 ground using event class selections that accommodate the broad range of sources of interest.

128 3. Sample Definition

129 We compiled a sample of all GRBs detected by the GBM between the beginning of
130 normal science operations of the *Fermi* mission on 2008 August 4th up to 2011 January 1st,
131 yielding a total of 620 GRBs. Of these, 288 bursts fell within 65° of the LAT z-axis (or

132 boresight) at the time of GBM trigger, which we define as the LAT FOV. Bursts detected at
 133 angles greater than 65° at the time of the GBM trigger were not considered for this analysis,
 134 due to the greatly reduced sensitivity of the instrument for such large off-axis angles. A plot
 135 of the distribution of the LAT boresight angles at trigger time, T_0 , for all 620 bursts is shown
 136 in Figure 1. Roughly half (46%) of the GBM-detected GRBs fell within the LAT FOV at T_0 ,
 137 as expected given the relative sky coverage of the two instruments. These bursts make up
 138 the sample for which the photon flux upper limits described in the next section have been
 139 calculated. A complete list of the 288 bursts in the sample, their positions, their durations,
 140 and their LAT boresight angles is given in Table 1.

141 We defined a subsample of 92 bursts which had a rate trigger greater than 75 counts
 142 s^{-1} in at least one of the two BGO detectors. This criteria is similar to the one adopted
 143 by Bissaldi et al. (2011) in their analysis of the brightest GBM detected bursts in the first
 144 year of observations. Hereafter, we refer to these 92 bursts as the “bright BGO subsample”;
 145 it comprises likely candidates for which it would be possible to find evidence of spectral
 146 curvature above the upper boundary of the nominal BGO energy window of ~ 40 MeV.
 147 Finally, we define our so-called “spectroscopic subsample” as the 30 bursts (of the bright
 148 BGO subsample) that have sufficient counts at higher energies to allow for the β index of a
 149 Band function fit to be determined with standard errors ≤ 0.5 . This spectroscopic subsample
 150 was used in joint fits with the LAT data to test models containing spectral breaks or cut-offs.

151 4. Analysis

152 4.1. LAT Upper Limits

153 We derive upper limits for the 288 GRBs that were detected by the GBM and fell in
 154 the LAT FOV from the LAT data using two methods. The first consists of the standard un-
 155 binned likelihood analysis using the software developed and provided by the LAT team, while
 156 the second method simply considers the total observed counts within an energy-dependent
 157 acceptance cone centered on the GBM burst location. The likelihood analysis will give more
 158 constraining upper limits, but since it uses the instrumental point-spread-function (PSF) in-
 159 formation to model the spatial distribution of the observed photons, in cases where the burst
 160 location is inaccurate and burst photons are present, it can give less reliable constraints. The
 161 latter method will be less constraining in general, but it will also be less sensitive to errors
 162 in the burst location, as the analysis considers photons collected over a fixed aperture and
 163 does not otherwise use the burst or photon positions on the sky. We use both methods to
 164 obtain photon flux upper limits over a 0.1–10 GeV energy range.

165 For the unbinned likelihood analysis, we used the standard software package provided
 166 by the LAT team, (ScienceTools version v9r15p6)¹. We selected “transient” class events
 167 in a 10° acceptance cone centered on the burst location, and we fit the data using the
 168 `pyLikelihood` module and the `P6_V3_TRANSIENT` response functions (Atwood et al. 2009).
 169 Each burst is modeled as a point source at the best available location, derived either from an
 170 instrument with good localization capabilities (e.g. *Swift* or LAT) or by the GBM alone. Of
 171 the 288 GRBs considered here, , In the likelihood fitting, the expected distribution of counts
 172 is modeled using the energy-dependent LAT PSF and a power-law source spectrum. The
 173 photon index of the power-law is fixed to either the β value found from the fit of the GBM
 174 data for that burst or, if the GBM data are not sufficiently constraining (i.e. $\delta\beta \leq 0.5$), to
 175 $\beta = -2.2$, the mean value found for the population of BATSE-detected bursts (Kaneko et al.
 176 2006; Preece et al. 2000a). An isotropic background component is included in the model,
 177 and the spectral properties of this component are derived using an empirical background
 178 model (Abdo et al. 2009c) that is a function of the position of the source in the sky and
 179 the position and orientation of the spacecraft in orbit. This background model accounts
 180 for contributions from both residual charged particle backgrounds and the time-averaged
 181 celestial gamma-ray emission.

182 Since we are considering cases where the burst flux in the LAT band will be weak or
 183 zero, the maximum likelihood estimate of the source flux may actually be negative owing to
 184 downward statistical fluctuations in the background counts. Because the unbinned likelihood
 185 function is based on Poisson probabilities, a prior assumption is imposed that requires the
 186 source flux to be non-negative. This is necessary to avoid negative probability densities that
 187 may arise for measured counts that are found very close to the GRB point-source location
 188 because of the sharpness of the PSF. On average, this means that for half of the cases in the
 189 null hypothesis (i.e., zero burst flux), the “best-fit” value of the source flux is zero but does
 190 not correspond to a local maximum of the unconstrained likelihood function (Mattox et al.
 191 1996).

192 Given the prior of the non-negative source flux, we treat the resulting likelihood func-
 193 tion as the posterior distribution of the flux parameter. In this case, an upper limit may be
 194 obtained by finding the flux value at which the integral of the normalized likelihood corre-
 195 sponds to the chosen confidence level (Amsler et al. 2008). For a fully Bayesian treatment,
 196 one would integrate over the full posterior distribution, i.e., marginalize over the other free
 197 parameters in the model. However, in practice, we have found it sufficient to treat the pro-
 198 file likelihood function as a one-dimensional probability distribution function (pdf) in the

¹<http://fermi.gsfc.nasa.gov/ssc/>

199 flux parameter. Again, in the limit of Gaussian statistics and a strong source, this method
 200 is equivalent to the use of the asymptotic standard error for defining confidence intervals.
 201 Hereafter, we will refer to this treatment as the “unbinned likelihood” method.

202 In the second set of upper limit calculations, we implement the method described by
 203 Helene (1983) and the interval calculation implemented in Kraft et al. (1991). Here, the
 204 upper limit is computed in terms of the number of counts and is based on the observed and
 205 estimated background counts within a prescribed extraction region. For the LAT data, the
 206 extraction region is an energy-dependent acceptance cone centered on the burst position.
 207 Since the burst locations from the GBM data have typical systematic uncertainties $\sim 3.2^\circ$
 208 (Connaughton et al. 2011), the size of the acceptance cone at a given energy is taken to be
 209 the sum in quadrature of the LAT 95% PSF containment angle and the total (statistical +
 210 systematic) uncertainty in the burst location. The counts upper limits are evaluated over a
 211 number of energy bands, converted to fluxes using the energy-dependent LAT exposure at
 212 the burst location, and then summed to obtain the final flux limit. Since this method relies
 213 on comparing counts without fitting any spectral shape parameters, we will refer to this as
 214 the “counting” method.

215 The time intervals over which the upper limits are calculated are important for their
 216 interpretation. For both upper limit methods, we consider three time intervals: two fixed
 217 intervals of 30 and 100 seconds post-trigger, and a “T100” interval that is determined through
 218 the use of the Bayesian Blocks algorithm (Jackson et al. 2005) to estimate the duration of
 219 burst activity in the NaI detector that has the largest signal above background. For the
 220 T100 interval, an estimate of the time-varying background count rate is obtained by fitting
 221 a 3rd degree polynomial to the binned data in time intervals outside of the prompt burst
 222 phase. Nominally, we take $T_0 - dt$ to $T_0 - 100$ s and $T_0 + 150$ s to $T_0 + dt$, where T_0 is the GBM
 223 trigger time and $dt = 200$ s, although we increased the separation of these intervals in some
 224 cases to accommodate longer bursts. The counts per bin is then subtracted by the resulting
 225 background model throughout the $T_0 - dt$ to $T_0 + dt$ interval, and the binned reconstruction
 226 mode of the Bayesian Blocks algorithm is applied. The T100 interval is then defined by the
 227 first and last change points in the Bayesian Blocks reconstruction.

228 The two fixed time intervals have been introduced so as to not bias our results through
 229 assumptions regarding the durations of the high energy components. The brighter LAT-
 230 detected GRBs have exhibited both delayed and extended high-energy emission on time
 231 scales that exceed the durations traditionally defined by observations in the keV–MeV energy
 232 range (Abdo et al. 2011). Hence, we search for and place limits on emission over intervals
 233 that may in some cases exceed the burst duration. We will discuss the implications of the
 234 limits found for the various time intervals in section 5.1.

4.2. GBM Spectroscopy

235

236 For the 92 bursts in the bright BGO subsample, we performed spectral fits to the
 237 NaI and BGO data and estimated the flux expected to be seen by the LAT between 0.1-
 238 10 GeV using the GBM fitted Band function (Band et al. 1993) parameters. The selection
 239 of background and source intervals for all bursts were performed manually through the use
 240 of the RMFIT (version 3.3) spectral analysis software package². Because the number of
 241 counts in the highest BGO energy bins is often in the Poisson regime, we use the Castor
 242 modification (Castor 1995) to the Cash statistic (Cash 1976), commonly referred to as C-Stat
 243 ³, since the standard χ^2 statistic is not reliable for low counts. The variable GBM background
 244 for each burst is determined for all detectors individually by fitting an energy-dependent,
 245 second order polynomial to the data several hundred seconds before and after the prompt
 246 GRB emission. The standard 128 energy bin CSPEC data (Meegan et al. 2009b) from the
 247 triggered NaI and BGO detectors were then fit from 8 keV to 1 MeV and from 200 keV to
 248 40 MeV, respectively, for each burst.

249 As we noted above, only 30 bursts in the bright BGO subsample have sufficient signal-
 250 to-noise to constrain the high-energy power-law index β of the Band function to within ± 0.5 .
 251 Although we considered a variety of models in our spectral analysis, we found that the Band
 252 function was sufficient to describe the spectral shape for all of these bursts.

253

5. Results

254

5.1. LAT Upper Limits

255 Of the 288 GRBs in our sample, we were able to obtain upper limits, at 95% confidence
 256 level (CL), for 270 bursts using the unbinned likelihood method and 95% CL upper limits
 257 for 250 bursts using the counting method for the T100 intervals derived from the GBM data.
 258 The GRBs for which upper limits could not be calculated were bursts that occurred either
 259 during spacecraft passages through the South Atlantic Anomaly (SAA) or at angles with
 260 respect to the Earth’s zenith that were $\gtrsim 100^\circ$, thereby resulting in diffuse emission at the
 261 burst locations that was dominated by γ -rays from the Earth’s limb produced by interactions
 262 of cosmic rays with the earth’s atmosphere. These cases where the burst occurred at a high
 263 angle with respect to the zenith primarily affects the counting method, because it requires

²<http://fermi.gsfc.nasa.gov/ssc/data/analysis/user/>

³<http://heasarc.nasa.gov/xanadu/xspec/manual/manual.html>

264 a reliable estimate of the background during the burst, and our method to estimate the
 265 background does not account for Earth limb emission. The likelihood method can fit for
 266 an Earth limb as a diffuse component, but it may give weaker limits since the background
 267 level is not as tightly constrained in this case compared to when the empirical background
 268 estimate can be used to model all of the non-burst emission. The photon flux upper limits
 269 found for the likelihood method for all three time intervals are presented in the last three
 270 columns of Table 1.

271 The distributions of the 95% CL photon flux upper limits obtained via the likelihood
 272 and counting methods for the 30s, 100s, and T100 time intervals are shown in upper-left,
 273 upper-right, and lower-left panels of Figure 2, respectively. As expected, the likelihood limits
 274 are systematically deeper than those found using the counting method over the same time
 275 interval. For either method, the upper limits for the 100s integrations are roughly half an
 276 order-of-magnitude deeper than for the 30s integrations. In the photon-limited case, this is
 277 expected since the flux limit at a specified confidence level should be inversely proportional
 278 to the exposure. The doubly peaked upper limits distribution that appears in the upper-
 279 left panel of Figure 2 for the T100 duration reflects the bimodal duration distribution for
 280 the short and long GRB populations. The median of the T100 upper limit distribution
 281 for the likelihood method is $\tilde{F}_{UL,T100} = 1.20 \times 10^{-4}$ photons $\text{cm}^{-2} \text{s}^{-1}$ with a standard
 282 deviation of $\sigma_{T100} = 1.57 \times 10^{-3}$; whereas the counting method distribution has a median of
 283 $\tilde{F}_{UL,T100} = 1.27 \times 10^{-4}$ photons $\text{cm}^{-2} \text{s}^{-1}$ and $\sigma_{T100} = 1.52 \times 10^{-3}$. The median of the 30s
 284 upper limits distribution for the likelihood method is $\tilde{F}_{UL,30s} = 4.76 \times 10^{-5}$ photons $\text{cm}^{-2} \text{s}^{-1}$
 285 with a standard deviation of $\sigma_{30s} = 3.20 \times 10^{-4}$; whereas the counting method distribution
 286 has a median of $\tilde{F}_{UL,30s} = 5.46 \times 10^{-5}$ photons $\text{cm}^{-2} \text{s}^{-1}$ and $\sigma_{30s} = 3.00 \times 10^{-4}$. The median
 287 of the 100s upper limits distribution for the likelihood method are $\tilde{F}_{UL,100s} = 1.74 \times 10^{-5}$
 288 photons $\text{cm}^{-2} \text{s}^{-1}$ and $\sigma_{100s} = 1.23 \times 10^{-4}$ and $\tilde{F}_{UL,100s} = 2.59 \times 10^{-5}$ photons $\text{cm}^{-2} \text{s}^{-1}$ and
 289 $\sigma_{100s} = 1.06 \times 10^{-4}$ for the counting method.

290 A comparison of the likelihood and counting methods for all three time intervals for is
 291 shown in the lower-right panel of Figure 2. The scatter in the upper limits distribution for
 292 both methods is largely due to the range of angles at which the GRBs occurred with respect
 293 to the LAT boresight, resulting in different effective areas and hence different exposures for
 294 each burst. The LAT exposure as a function of the off-axis angle drops steeply with increasing
 295 inclination, resulting in a shallowing of the LAT upper limits as a function of increasing off-
 296 axis angle, which can be seen in Figure 3. Overall, the two methods give consistent results
 297 for the bursts in our sample, and therefore we will hereafter focus primarily on the limits
 298 obtained with the likelihood method in our discussion of the implication of these results.

299 Despite the dependence of the upper limit values on off-axis angle, the distribution

300 of LAT photon flux upper limits is relatively narrow for angles $< 40^\circ$, allowing us to
 301 define an effective LAT sensitivity assuming a typical GRB spectrum (i.e., $\beta \approx -2.2$).
 302 We can therefore set sensitivity thresholds for the corresponding median photon flux up-
 303 per limit for each integration time of $F_{\text{lim},30\text{s}} = 4.7 \times 10^{-5}$ photons $\text{cm}^{-2}\text{s}^{-1}$ and $F_{\text{lim},100\text{s}} =$
 304 1.6×10^{-5} photons $\text{cm}^{-2}\text{s}^{-1}$.

305 Finally, in Figure 4 we plot the location of each burst on the sky in Galactic coordinates,
 306 color-coded to represent the likelihood-determined photon flux upper limits. There is no
 307 evidence of a spatial dependence of the GBM detection rate nor of the magnitude of the
 308 LAT upper limit, as a function of Galactic latitude b .

309 5.2. GBM Spectral Fits and Upper Limit Comparisons

310 We compare the LAT upper limits calculated over the burst duration to the expected
 311 0.1–10 GeV photon fluxes found through extrapolations of spectral fits presented in the first
 312 GBM spectral catalog (Goldstein et al. in press). We focus this analysis on bursts for which
 313 a Band spectral model was a preferred fit compared to models with fewer degrees of freedom,
 314 since alternative models such as Comptonized spectra suffer sharp drops in expected flux
 315 at high-energy and are not expected to result in LAT detections without the presence of
 316 additional spectral components. Of the 487 GRBs presented in that catalog, a Band model
 317 fit was preferred over simpler models for 161 bursts, 75 of which appeared in the LAT field
 318 of view. For this comparison, the LAT upper limits were recalculated for a duration that
 319 matched the interval used in the GBM spectral catalog (see Goldstein et al. 2011 for a
 320 detailed discussion of their interval selection). We next performed a simulation in which we
 321 varied the expected LAT photon flux fitted values using the associated errors for each burst
 322 in order to determine the median number of bursts over all realizations that would fall above
 323 the LAT upper limit. In a total of 10^5 realizations, we find that 50% of the GRBs in the
 324 GBM spectral catalog, which prefer a Band model fit, have expected 0.1–10 GeV photon
 325 fluxes that exceeds the LAT upper limit.

326 We investigate the differences between the GBM-based extrapolations and the LAT
 327 upper-limits further by performing detailed spectral fits to our spectroscopic subsample.
 328 The spectral parameters obtained from the fits to the GBM data only for the 30 GRBs in
 329 this spectroscopic subsample are listed in Table 2. The median values of the low and high
 330 energy power-law indices and the peak of the νF_ν spectra are $\alpha = -0.83$, $\beta = -2.26$, and
 331 $E_{\text{pk}} = 164$ keV, with standard deviations of $\sigma_\alpha = 0.44$, $\sigma_\beta = 0.25$, and $\sigma_{E_{\text{pk}}} = 177$ keV,
 332 respectively. The distributions of spectral parameters for these bursts are consistent with
 333 similar distributions found for BATSE-detected GRBs (Kaneko et al. 2006; Preece et al.

2000a). The time durations used in the spectral fits and the time-averaged photon flux values in the 0.02–20 MeV energy range for these GRBs are given in Table 3. In the third column, we list the expected flux in the 0.1–10 GeV energy range assuming a power-law extrapolation of the Band function fit to the GBM data; and in the fourth column, we give the measured LAT photon flux upper limit found for the same time interval. The errors on the expected LAT photon fluxes were determined using the covariance matrices obtained from the GBM spectral fits.

A comparison of the LAT photon flux upper limits versus the expected 0.1–10 GeV photon fluxes for each burst in our spectroscopic subsample is shown as blue data points in Figure 5. The downward arrows on the expected flux values indicate values that are consistent with zero within the $1\text{-}\sigma$ errors shown. The dashed line represents the line of equality between the expected LAT photon flux and the LAT photon flux upper limits when calculated for the durations presented in Table 5. In a total of 10^5 realizations, we find that 53% of GRBs in our spectroscopic subsample have expected 0.1–10 GeV photon fluxes that exceed their associated 95% CL LAT upper limit. As with the flux comparison, roughly 50% in our sample also have expected fluence values that exceed the 95% CL LAT fluence upper limit. Figure 6 shows that the degree to which the expected flux in the LAT energy range from these bursts exceed our estimated LAT upper limits correlates strongly with the measured high energy spectral index, with particularly hard bursts exceeding the estimated LAT sensitivity by as much as a factor of 100. Again, the spectral fits to the bright bursts detected by the BGO clearly shows that a simple extrapolation from the GBM band to the LAT band systematically over-predicts the observed flux.

5.3. Joint GBM and LAT Spectral Fits

Including the LAT data in the spectral fits drastically alters the best-fit Band model parameters and the resulting expected photon flux in the LAT energy range. The best-fit parameters of the joint spectral fits for the spectroscopic subsample can be found in Table 4. The high-energy spectral indices are typically steeper (softer) than found from fits to the GBM data alone.

The difference in the β values for the joint fits with respect to the fits to the GBM data alone can be found in Column 8 of Table 4. The resulting β distributions are shown in Figure 7. The GBM-only β distribution (red histogram) peaks at $\beta = -2.2$, matching the β distribution found for the population of BATSE-detected bursts presented in Preece et al. (2000a). In contrast, the β distribution found from the joint fits (blue histogram) indicates spectra that are considerably softer, with a median value of $\beta = -2.5$. While the GBM-

368 only β distribution includes 5 GRBs with $\beta > -2.0$, no bursts had β values this hard from
 369 the joint fits. The low energy power-law index α and the peak of the νF_ν spectra, E_{pk}
 370 distribution remain relatively unchanged. In Figure 5, we compare the LAT photon flux
 371 upper limits calculated over the burst duration presented in Table 4 versus the expected
 372 0.1–10 GeV photon fluxes for each burst, now using a power-law extrapolation of the Band
 373 function that was fit to both the GBM and LAT data. The softer β values obtained through
 374 the joint fits yield expected LAT photon flux values that are more consistent with the LAT
 375 non-detections, with only 23% of the bursts in our spectroscopic subsample with expected
 376 flux values that exceed the 95% CL LAT flux upper limit given 10^5 realizations of the data
 377 about their errors. We find that a similar ratio of bursts have expected fluence values that
 378 exceed their associated 95% CL LAT fluence upper limit.

379 5.4. Spectral Breaks or Softer Spectral Indices?

380 Although the discrepancy between the predicted 0.1–10 GeV fluxes from the GBM-
 381 only fits and the LAT upper limits can be explained by the softer β values in the joint
 382 fits, intrinsic spectral breaks at energies $\gtrsim 40$ MeV can also reconcile the conflicting GBM
 383 and LAT results. Determining whether softer β values or spectral breaks are present has
 384 at least two important implications: If the spectral breaks or cut-offs arise from intrinsic
 385 pair production ($\gamma\gamma \rightarrow e^+e^-$) in the source, then the break or cut-off energy would provide
 386 a direct estimate of the bulk Lorentz factor of the emitting region within the outflow. On
 387 the other hand, an intrinsically softer distribution of β values would mean that theoretical
 388 inferences based on the β distributions found by fitting BATSE or GBM data alone may
 389 need to be revised. Evidence for either spectral breaks or softer β values could also provide
 390 support for multi-component models that have been used to describe novel spectral features
 391 detected by the GBM and LAT (e.g., Guiriec et al. 2011a).

392 For the joint fitting of the GBM and LAT data, deciding between the two possibilities
 393 for any single burst can be cast as a standard model selection problem. Under the null
 394 hypothesis, we model the GRB spectrum using a simple Band function, as we have done in
 395 section 5.3. As an alternative hypothesis, we could extend the Band model to account for
 396 the presence of a spectral break. This may be done via an additional break energy above the
 397 Band E_{pk} , effectively using a doubly broken power-law in the fit; or it could be accomplished
 398 by adding an exponential cut-off to the Band model with cut-off energy $E_c > E_{\text{pk}}$. In either
 399 case, the null and alternative hypotheses are “nested” such that the former is a special case of
 400 the latter for some values of the extra model parameters that are introduced. Assuming there
 401 are n_{alt} additional free parameters under the alternative model, then whether the alternative

402 model is statistically preferred would be given by the $\Delta\text{C-Stat}$ value assuming it follows a
 403 χ^2 distribution for n_{alt} degrees-of-freedom.

404 For the purposes of this analysis, we have adopted an alternative model consisting of
 405 a Band function plus a step function fixed at 50 MeV. Although unphysical, a simple step
 406 function introduces a single additional degree-of-freedom and can adequately represent the
 407 need for a break in the high-energy spectra. This additional degree-of-freedom represents the
 408 normalization of the Band function’s high-energy component above 50 MeV, which is left to
 409 vary, leading to the normalization of the power-law above 50 MeV being adjusted such that it
 410 is always consistent with the LAT upper limits. For this analysis, the index of the power-law
 411 above the break is fixed to match the Band function’s high-energy power-law index, which is
 412 allowed to vary as a free parameter. Since this introduces a single extra degree-of-freedom, a
 413 value of $\Delta\text{C-Stat} > 9$ would represent a 3σ improvement in the fit. We adopt this criterion
 414 as the threshold for a statistical preference for a break in the high-energy spectrum of an
 415 individual GRB.

416 An example of such a fit can be seen in Figure 8, where the three panels show (clockwise)
 417 a Band model fit to GBM data alone, a Band model fit to both the GBM and LAT data, and
 418 a Band model plus a step function fit to the GBM and LAT data. The difference between
 419 the first two panels demonstrates the degree to which the high-energy spectral index can
 420 steepen to accommodate the LAT data, despite being outside of the range allowed by the
 421 statistical uncertainty in the β determination made through the GBM fit alone. The third
 422 panel shows the effect of introducing a step function between the two instruments, in which
 423 the requirement for a softer β value is alleviated. For the fit shown in Figure 8, the β value
 424 determined through the Band model plus a step function fit is consistent with the value
 425 found by fitting a Band model to the GBM data alone.

426 The $\Delta\text{C-Stat}$ values obtained for the Band and Band+step function fits are listed in
 427 Column 9 of Table 4. For most of the bursts, a simple steepening of the high energy power-
 428 law index was sufficient to explain the lack of a LAT detection. However, in 6 cases $\Delta\text{C-Stat}$
 429 exceeded a value of 9, indicating a statistical preference for a break in the high energy
 430 spectrum. Figure 9 shows the ratio of the expected LAT flux (based on GBM-only fits)
 431 to the LAT 95% CL upper limit plotted versus the $\Delta\text{C-Stat}$ values for the spectroscopic
 432 subsample. A weak correlation between the flux ratio and $\Delta\text{C-Stat}$ is apparent. In addition,
 433 Figure 10 shows an anti-correlation between the resulting $\Delta\text{C-Stat}$ values for this sample
 434 plotted versus the uncertainty in the high-energy spectral index found from fits to the GBM
 435 data alone. The bursts for which a spectral break is statistically preferred both have the
 436 most severe discrepancies between the GBM-only extrapolations and the LAT upper limits
 437 and also have the smallest uncertainties in their GBM-only β values.

5.5. Constraints on the Bulk Lorentz Factor

438

439 If we assume that the high-energy spectra in the 6 GRBs that prefer spectral cut-offs
 440 are a result of $\gamma\gamma$ attenuation, as opposed to a spectral turnover that is intrinsic to the
 441 GRB spectrum, then we can use the joint GBM and LAT spectral fits in conjunction with
 442 the LAT non-detections at 100 MeV to place limits on the maximum Lorentz factor. In
 443 this context, the high-energy γ -rays produced within the GRB jet may undergo $\gamma\gamma \rightarrow e^+e^-$
 444 pair production and can be absorbed *in situ*. The interaction rate of this process and
 445 corresponding optical depth, $\tau_{\gamma\gamma}$, depend on the target photon density and can be significant
 446 when both the high-energy and target photons are produced in the same physical region.
 447 Highly relativistic bulk motion of such an emission region can reduce the implied $\gamma\gamma$ optical
 448 depth greatly by allowing for a larger emitting region radius and a smaller target photon
 449 density for a given observed flux and variability time scale. Observation of γ -ray emission
 450 up to an energy $E_{\max} \gg m_e c^2$ thus can be used to put a lower limit on the bulk Lorentz
 451 factor Γ of the emitting region (Ackermann et al. 2010b; Granot et al. 2008; Lithwick & Sari
 452 2001; Razzaque et al. 2004). This method is valid for $\Gamma \leq E_{\max}(1+z)/m_e c^2$, which follows
 453 from the threshold condition for e^+e^- pair production, when both the incident and target
 454 photons are at the maximum observed energy.

455 If a high-energy γ -ray photon with energy E and the observed broadband photon emis-
 456 sion originate from the same physical region, and if we assume the photons are quasi-isotropic
 457 in the comoving frame, then the $\gamma\gamma \rightarrow e^+e^-$ pair production optical depth can be written as

$$\tau_{\gamma\gamma}(E) = \frac{3}{4} \frac{\sigma_T d_L^2}{t_v \Gamma} \frac{m_e^4 c^6}{E^2 (1+z)^3} \int_{\frac{m_e^2 c^4 \Gamma}{E(1+z)}}^{\infty} \frac{d\epsilon'}{\epsilon'^2} n \left(\frac{\epsilon' \Gamma}{1+z} \right) \varphi \left[\frac{\epsilon' E (1+z)}{\Gamma} \right]. \quad (1)$$

458 Here $n(\epsilon)$ is the observed photon spectrum, ϵ is the target photon energy, ϵ' is the target
 459 photon energy in the comoving frame of the emitting plasma, d_L is the luminosity distance,
 460 t_v is the γ -ray flux variability time scale, and σ_T is the Thomson cross-section. The function
 461 $\varphi[\epsilon' E (1+z)/\Gamma]$ is defined by Gould & Schröder (1967) and Brown et al. (1973). The value of
 462 $\Gamma_{\gamma\gamma, \min}$ follows from the condition $\tau_{\gamma\gamma}(E_{\max}) = 1$. This single-zone model, in which the spatial
 463 and temporal dependancies of $\tau_{\gamma\gamma}$ have been averaged out, has been the technique used to
 464 measure the reported values of $\Gamma_{\gamma\gamma, \min}$ for the LAT detections of GRBs 080916C, 090510,
 465 and 09092B in Abdo et al. (2009d), Ackermann et al. (2010b), and Abdo et al. (2009b),
 466 respectively.

467 A direct estimate of the bulk Lorentz factor Γ , as opposed to a minimum value, of the
 468 GRB jet can be made based on evidence of a cut-off in the spectral fits that are attributed
 469 to $\gamma\gamma$ attenuation, such as has been reported for GRB 090926A in Abdo et al. (2010).

470 In the case of the 6 GRBs that we are considering here for which no direct evidence

471 for a spectral cut-off is otherwise detected, we use our upper limits to calculate a maximum
 472 bulk Lorentz factor $\Gamma_{\gamma\gamma,\max}$ from the condition $\tau_{\gamma\gamma}(E_{\text{UL}}) = 1$. To do so, we use the Band
 473 function fit to the GBM and LAT data and set $E_{\text{UL}} = 100$ MeV. We also assume a variability
 474 time scale of $t_v = 0.1$ s, which we believe represents a conservative estimate of t_v given the
 475 ubiquity of millisecond variability in BATSE detected GRBs (Walker et al. 2000) as well as
 476 the short timescales observed in other LAT detected GRBs (Ackermann et al. 2010b).

477 We note that if the cutoff energy due to intrinsic pair opacity is small enough, $E_{\text{cutoff}} <$
 478 $m_e c^2 \Gamma / (1+z)$, then the Thomson optical depth of the pairs that are produced in the emitting
 479 region is $\tau_{T,e^\pm} > 1$ (Abdo et al. 2009a; Lithwick & Sari 2001). This should affect both
 480 the observed spectrum, thermalizing it for a large enough optical depth, and light curve,
 481 eliminating short timescale variability. For $E_{\text{cutoff}} = 100$ MeV, this condition is nearly
 482 violated at $z \lesssim 1.0$, therefore a much lower cutoff energy would be hard to reconcile with an
 483 intrinsic pair opacity origin for GRBs at low redshift.

484 The resulting $\Gamma_{\gamma\gamma,\min}$ and $\Gamma_{\gamma\gamma,\max}$ values for previously reported LAT detections and
 485 from the upper limits presented here are shown in Figure 13. Since the Lorentz factor
 486 calculation depends on the redshift, which is unknown for the majority of GBM detected
 487 bursts, we have plotted the $\Gamma_{\gamma\gamma,\max}$ values as a function of the redshift (red lines). One GRB
 488 in our spectroscopic subsample, GRB 091127, has a measured redshift which allows us to
 489 constrain the burst’s Γ_{\max} value. Using a redshift of $z = 0.490$ (Cucchiara et al. 2009) and
 490 $E_{\text{UL}} \sim 100$ MeV, we calculate a relatively small bulk Lorentz factor of $\Gamma_{\max} \sim 155$. Using
 491 the measurements of E_{UL} for these GRBs provides a relatively narrow distribution of Γ_{\max}
 492 that range from $50 < \Gamma_{\max} < 300$ at $z = 1$ to $400 < \Gamma_{\gamma\gamma,\max} < 640$ at $z = 4$. These values
 493 stand in stark contrast to the LAT detected GRBs for which $\Gamma_{\gamma\gamma,\min}$ was measured, all of
 494 which have $\Gamma_{\gamma\gamma,\min} > 800$.

495 The detection of spectral curvature by the LAT in the spectrum of GRB 090926 provides
 496 a case that appears to bridge the LAT detected and non-detected samples. The estimate
 497 of Γ of 200–700 presented in Abdo et al. (2010) reflects the systematic differences between
 498 Lorentz factors obtained through the use of time-dependent models by Granot et al. (2008)
 499 which yield systematic differences in $\tau_{\gamma\gamma}$ and the inferred Γ when compared to the simple
 500 single-zone model used above. Granot et al. (2008), and more recently Hascoët et al. (2011),
 501 have shown that such time-dependent models, which include the temporal evolution of $\tau_{\gamma\gamma}$
 502 during the emission period, can yield inferred Γ estimates that are reduced by a factor of
 503 2-3 compared to estimates made using single-zone models. In the context of these time-
 504 dependent model, the $\Gamma_{\gamma\gamma,\min}$ and $\Gamma_{\gamma\gamma,\max}$ presented in Figure 13 would all be systematically
 505 overestimated by a factor of 2-3, but the dichotomy between the LAT detected and LAT non-
 506 detected GRBs would persist since all Γ estimates would be effected by the same correction.

507 Note that the grey dashed line in Figure 13 demarcates the self-consistency line where
 508 the condition that $\Gamma \leq E_{\text{max}}(1+z)/m_e c^2$ is violated, implying an incorrect determination of
 509 $\tau_{\gamma\gamma}$, for the bursts with no detected emission above $E_{\text{max}} = 100$ MeV. None of the bursts in
 510 our spectroscopic subsample violate this condition at any redshift for the choice of $E_{\text{cutoff}} =$
 511 100 MeV.

512 6. Discussion

513 The upper limits presented above place stringent constraints on the high energy emission
 514 from GRBs detected by the GBM. Of the 620 bursts detected by the GBM from 2008 August
 515 4th to 2011 January 1st, 46% were within the LAT FOV. There is evidence for high energy
 516 emission > 100 MeV in the LAT energy range for 23 GRBs, representing 8% of the entire
 517 GBM sample observed by the LAT. This is significantly less than the pre-launch estimate of
 518 1 detection per month that produces at least 100 counts above 100 MeV (Band et al. 2009).

519 The results of our joint GBM and LAT spectral fits show that both softer high-energy
 520 power-law spectra and spectral breaks likely account for the lower-than-expected number
 521 of LAT-detected GRBs. For the 24 bursts in our spectroscopic subsample where a spectral
 522 break is not statistically justified, the β values from the joint fits are systematically softer
 523 than the values found from fitting the GBM data alone. This may indicate that the high-
 524 energy spectral index for the Band model may in fact be softer than that deduced from
 525 measurements made by previous missions, such as BATSE, which had a much narrower
 526 energy range compared to the combined coverage of the GBM and LAT. The GBM+LAT β
 527 distribution shown in Figure 7 appears to exclude the harder spectra found from fits made
 528 with just the lower energy BATSE or GBM data. In fact, we find no cases of spectra with
 529 $\beta > -2.0$, which would otherwise result in a divergent energy flux at high energies.

530 The detection of softer β values also provides support for continuum models with mul-
 531 tiple components, which have been used to describe novel spectral features detected by the
 532 GBM and LAT. Recent work on bright GRBs by Guiriec et al. (2011a) suggests that al-
 533 though the Band function represents many GRB spectra very well in a limited energy range,
 534 it is sometimes possible to discern, even in this limited energy range, contributions such as
 535 thermal components in addition to the presumably non-thermal synchrotron emission rep-
 536 resented by the Band function. The addition of such components to a Band function has
 537 the effect of modifying the parameter values, in the case of GRB 100724B raising E_{pk} and
 538 softening β (Guiriec et al. 2011b). Whilst these more complex models are not statistically
 539 favored in most GRBs due to low photon statistics, their successful fits to some GRBs in-
 540 dicate that the representation of GRB emission by a Band function may be inadequate and

541 lead to overestimates of fluxes when extrapolated to GeV energies. Because the Band func-
 542 tion was developed to represent GRB spectra rather than to parametrize a physical model,
 543 it is difficult to decouple physical components from this empirical function, which probably
 544 incompletely describes elements of multiple physical phenomena. Additionally, the superpo-
 545 sition of Band functions does not necessarily produce a Band function, so the presence of
 546 spectral evolution means that any extrapolation to higher energies from flux-averaged spectra
 547 may not be representative of the emission throughout the entire GRB emission period.

548 Granot et al. (2008) have shown that even when integrating over a single spike in a light
 549 curve there is a steepening to a softer power-law rather than an exponential cutoff. This
 550 is due to the high-energy power law arising from the sum of instantaneous spectra with an
 551 exponential cutoff whose break energy evolves with time. Likewise, Hascoët et al. (2011)
 552 have shown that the effect of averaging a time variable opacity cutoff would be manifested
 553 as a steepening in the power-law index of the high-energy spectral slope rather than as a
 554 sharp cutoff in the spectrum. Likewise, Baring (2006) has shown that skin-depth effects tend
 555 to smear out exponential attenuation when the source and target photons originate in the
 556 same volume, resulting in a similar effect. Such considerations could explain the softer β
 557 values found when fitting both the GBM and LAT data, even in cases where a spectral break
 558 was not statistically preferred. Detailed time resolved spectroscopy of bright GBM detected
 559 GRBs should be able to discriminate between such pair opacity effects, intrinsically steeper
 560 high-energy spectra, or the more complex continuum models discussed above β (Guiriec et al.
 561 2011b).

562 The bursts in our spectroscopic subsample were chosen specifically because they were
 563 among the brightest bursts detected by the BGO and yet had no appreciable signal in the
 564 LAT. This makes them good candidates to examine for evidence of spectral breaks, but they
 565 may also form a biased data set. In order to understand how representative these bursts are
 566 of the general GRB population, we plot in Figure 11 the distribution of the time averaged
 567 photon flux as determined from fits to GBM data for bursts in our spectroscopic subsam-
 568 ple (red), the bursts which appear in the first GBM spectral catalog (gold) the bursts in
 569 the bright BATSE catalog presented in Kaneko et al. (2006) (green), and a sample of simu-
 570 lated BATSE bursts (blue) using the spectral parameter distributions given in Preece et al.
 571 (2000b). The resulting distributions show that the spectroscopic subsample is consistent
 572 with being drawn from the distribution of the brightest bursts detected by BATSE.

573 We extend this analysis in Figure 12, where we plot the expected 0.1–10 GeV LAT
 574 photon flux versus the 20–2000 keV photon flux for our spectroscopic sample using spectral
 575 parameters from the GBM-only fits (green) and from the joint GBM-LAT fits (red), along
 576 with the bursts from the first GBM spectral catalog which were in the LAT FOV (blue).

577 The color gradient in the GBM sample represents the burst’s duration, with darker (blue)
 578 symbols representing shorter duration bursts. In addition, we have plotted the 6 LAT-
 579 detected bursts (gold) that had spectra that could be fit with a single Band function (i.e.,
 580 we excluded bursts with extra high-energy components). The dashed line represents the
 581 median T100 upper limit. The green data points demonstrate how fits to the GBM data
 582 without the inclusion of the LAT data yield spectral parameters that over-predict the flux
 583 in the LAT energy range, which can be seen by the number of bursts in our spectroscopic
 584 subsample that fall above the median upper limit values. The red data points represent the
 585 predicted LAT flux for the same GRBs using spectral parameters determined through fits to
 586 both the GBM and LAT data. Roughly 50% of the bursts from the GBM spectral catalog fall
 587 above the median T100 upper limit. This would imply that a large fraction of bright GBM
 588 detected bursts would have been detectable by the LAT assuming a direct extrapolation
 589 of their high-energy spectra. Therefore, we conclude that intrinsic spectral breaks and/or
 590 softer-than-measured high-energy spectra must be fairly common in the GRB population in
 591 order to explain the lack of LAT-detected GRBs.

592 Despite the unknown distances to all but one of the GRBs in our spectroscopic sub-
 593 sample, the allowed range of $\Gamma_{\gamma\gamma,\max}$ values for $0 < z < 5$ all lie well below $\Gamma_{\gamma\gamma,\max} \sim 720$.
 594 This range of $\Gamma_{\gamma\gamma,\max}$ for the relativistic outflow contrasts with the minimum Lorentz factors
 595 that have been calculated for the bright, LAT-detected GRBs using their highest detected
 596 photons. For GRB 080916C, GRB 090510, and GRB 09092B, the estimated lower limits
 597 for the Lorentz factors were found to be 887, 1200, and 867 when using single zone models,
 598 respectively. Therefore, measurements of $\Gamma_{\gamma\gamma,\min}$ and $\Gamma_{\gamma\gamma,\max}$ from both LAT detections and
 599 non-detections reveal a wide distribution in the bulk Lorentz factor of GRB outflows, with
 600 a potential range of over ~ 10 .

601 As discussed above, these estimates of $\Gamma_{\gamma\gamma,\min}$ and $\Gamma_{\gamma\gamma,\max}$ have been calculated us-
 602 ing simple single-zone models, which may provide overestimated values compared to time-
 603 dependent multi-zone models that take into account the time variability of $\tau_{\gamma\gamma}$. In such a
 604 scenario, our estimates of the $\Gamma_{\gamma\gamma,\min}$ and $\Gamma_{\gamma\gamma,\max}$ would need to be rescaled downwards by
 605 a factor of 2–3, but the large difference between the LAT detected and non-detected GRBs
 606 would remain.

607 The *Fermi* LAT Collaboration acknowledges generous ongoing support from a number
 608 of agencies and institutes that have supported both the development and the operation of the
 609 LAT as well as scientific data analysis. These include the National Aeronautics and Space
 610 Administration and the Department of Energy in the United States, the Commissariat à
 611 l’Energie Atomique and the Centre National de la Recherche Scientifique / Institut National
 612 de Physique Nucléaire et de Physique des Particules in France, the Agenzia Spaziale Italiana

613 and the Istituto Nazionale di Fisica Nucleare in Italy, the Ministry of Education, Culture,
614 Sports, Science and Technology (MEXT), high-energy Accelerator Research Organization
615 (KEK) and Japan Aerospace Exploration Agency (JAXA) in Japan, and the K. A. Wallen-
616 berg Foundation, the Swedish Research Council and the Swedish National Space Board in
617 Sweden.

618 Additional support for science analysis during the operations phase is gratefully acknowl-
619 edged from the Istituto Nazionale di Astrofisica in Italy and the Centre National d'Études
620 Spatiales in France.

621 The *Fermi* GBM collaboration acknowledges support for GBM development, operations
622 and data analysis from NASA in the US and BMWi/DLR in Germany.

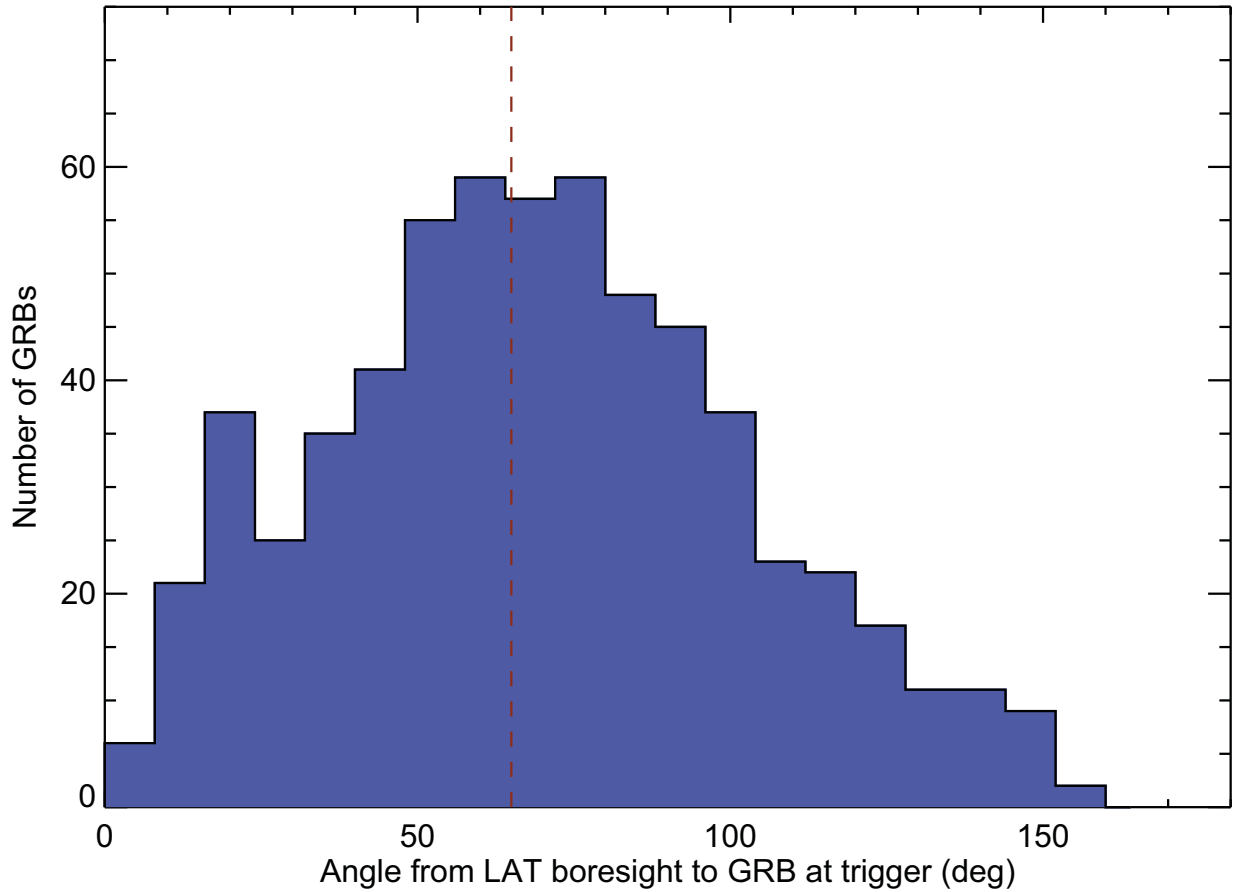


Fig. 1.— The distribution of LAT off-axis angles of the 620 bursts that triggered the GBM from 2008 August 4th to 2011 January 1st. The red dashed line at an off-axis angle of 65° indicates the nominal boundary of the LAT FOV. A total of 288 bursts (46% of all detected bursts) fell within the LAT FOV over this period.

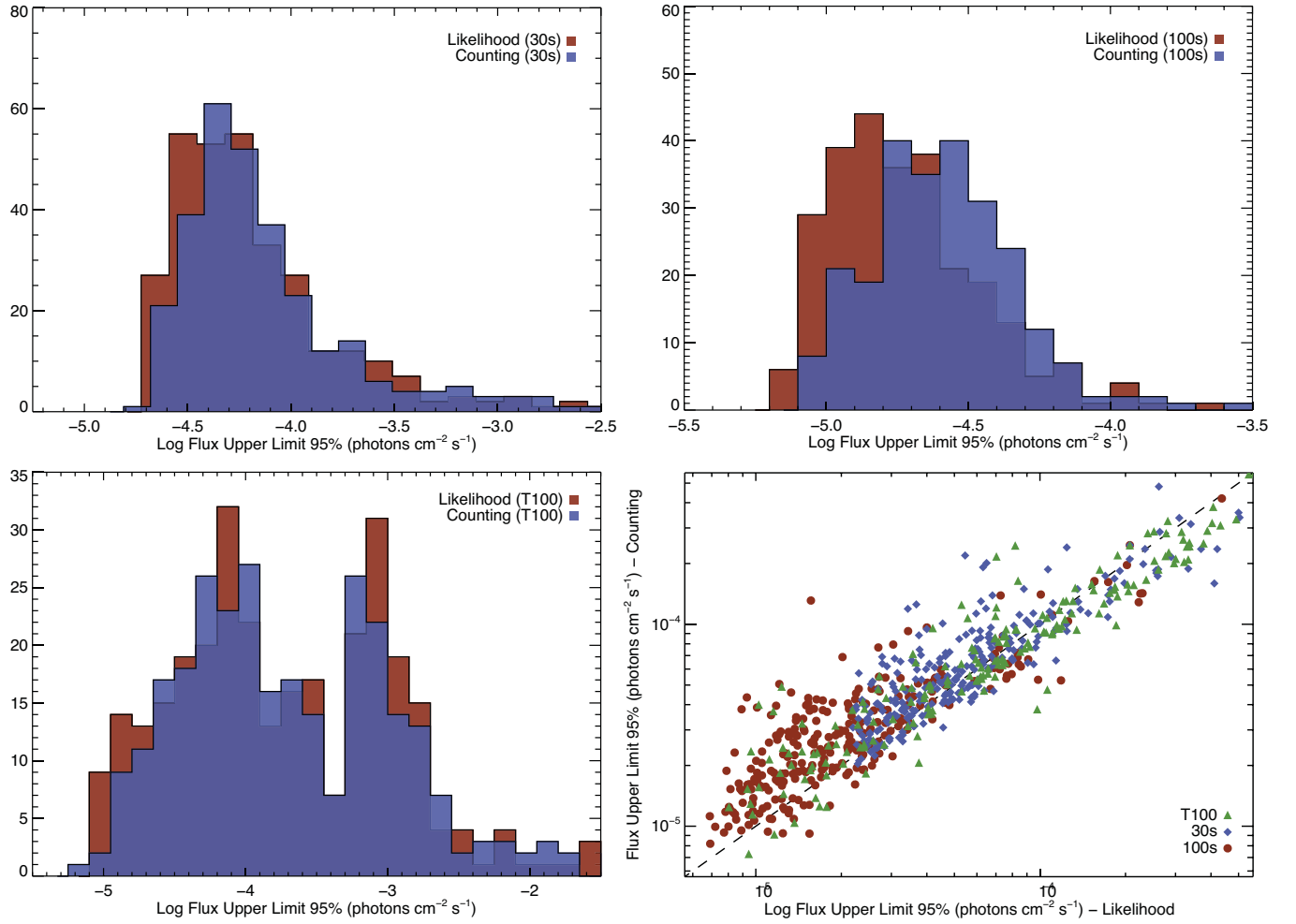


Fig. 2.— The distributions of the 95% CL photon flux upper limits obtained via the likelihood and counting methods for the 30 s (upper-left), 100 s (upper-right), and T100 (lower-left) time intervals. A scatter plot comparison of the upper limits calculated over the three intervals is shown in the lower-right panel. The dashed line represents the line of equality between the likelihood and counting methods.

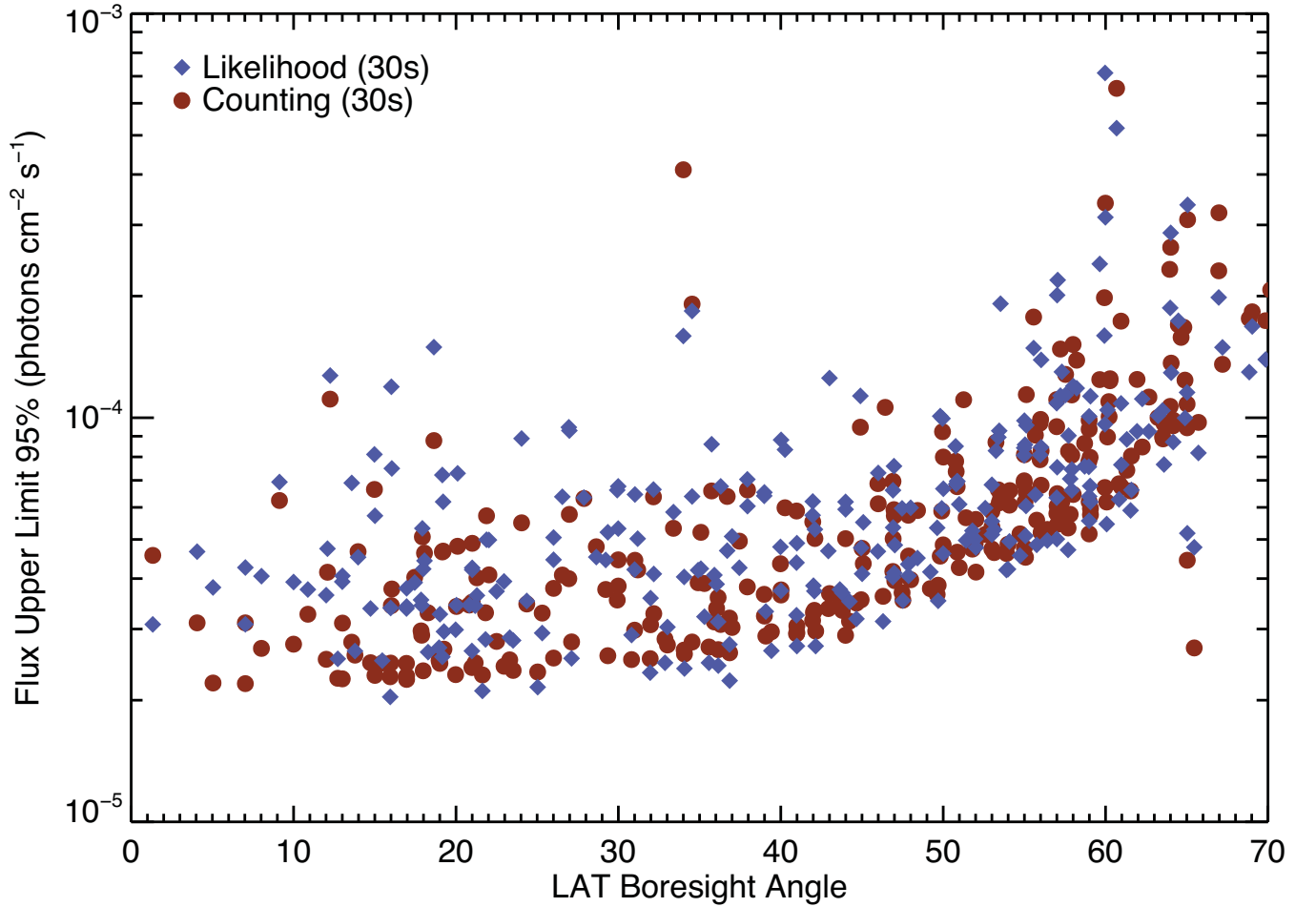
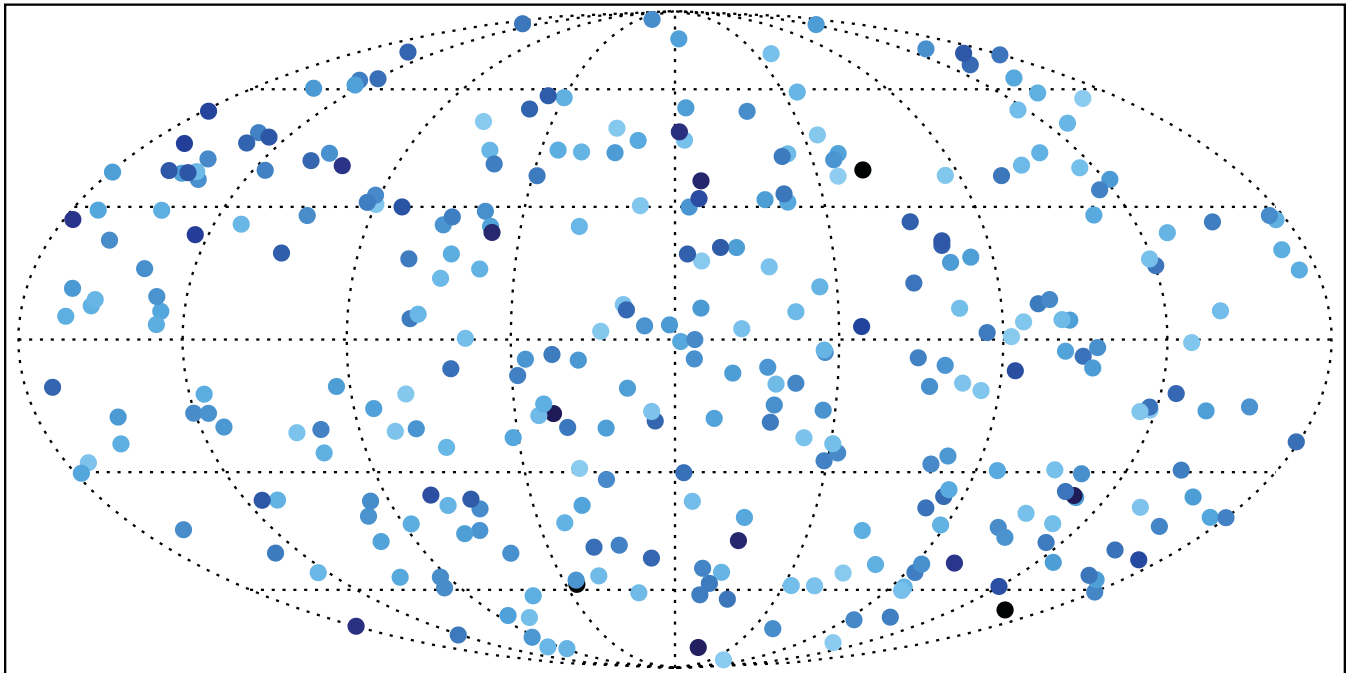


Fig. 3.— The 95% CL photon flux upper limits determined using the likelihood and counting methods as a function of off-axis angle. The decreasing exposure as a function of off-axis angle results in the shallowing of the LAT upper limits for bursts occurring away from the LAT bore sight.

GBM Detections & LAT Flux Upper Limits – Galactic Coordinates



Log Flux Upper Limit 95% (photons $\text{cm}^{-2} \text{s}^{-1}$) – Likelihood Method



Fig. 4.— The celestial distribution of 288 gamma-ray bursts as detected by *Fermi*-GBM in the first 2.5 years of LAT operations that fell in the LAT FOV, plotted in Galactic coordinates. The colors represents the 95% CL LAT photon flux upper limits.

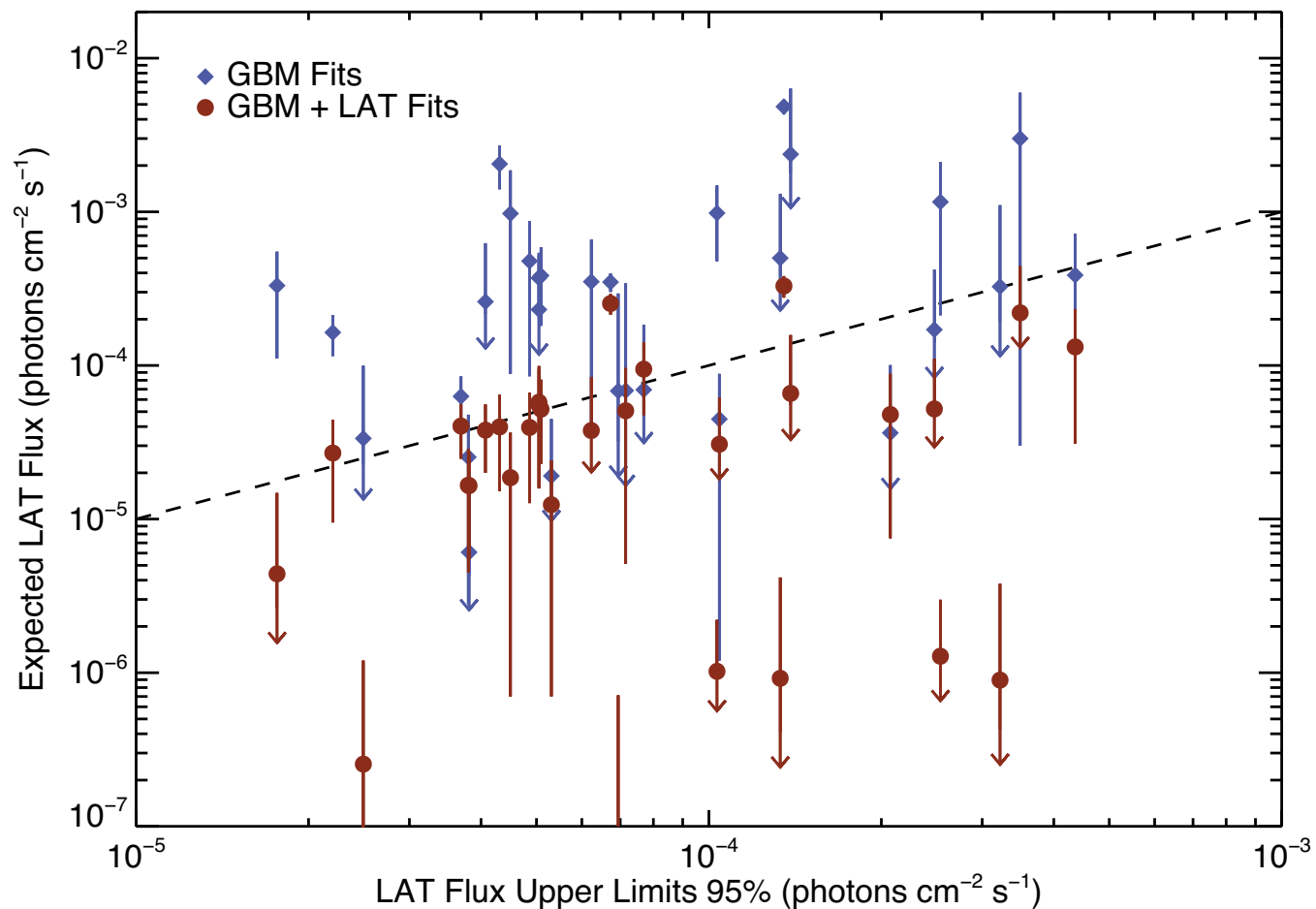


Fig. 5.— The expected photon flux, based on fits to the prompt GBM spectrum and duration plotted versus the LAT flux upper limit for each burst. When fitting only to the GBM data, roughly 50% of the bursts in the spectroscopic sample have expected LAT fluxes that exceed the LAT 95% CL flux upper limit. When fitting both the GBM and LAT data, only 23% of our sample have expected flux values that exceed the 95% CL LAT flux upper limit. The dashed line represents the line of equality.

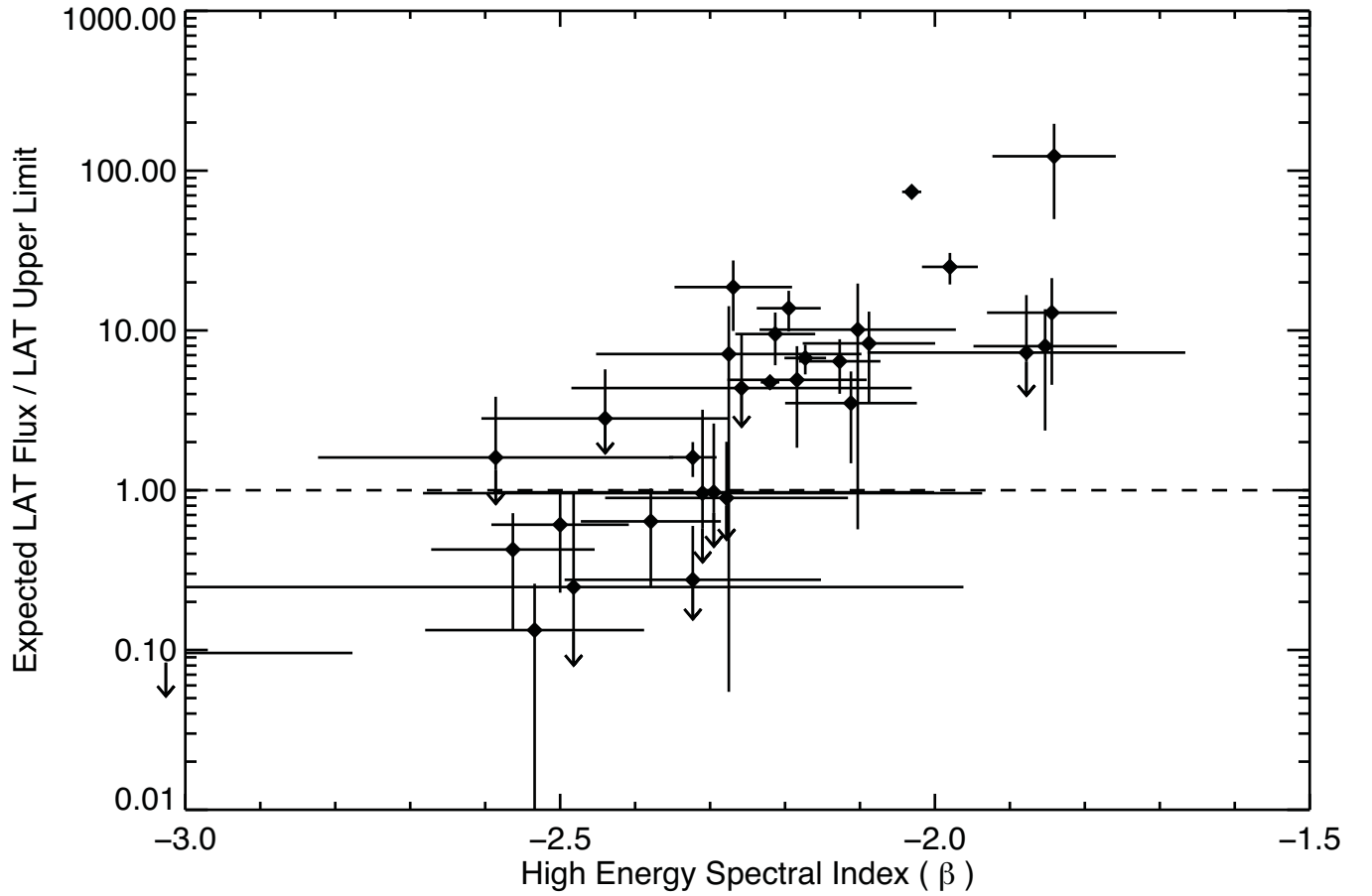


Fig. 6.— The ratio of the expected LAT flux, based on fits to the prompt GBM spectrum, to the LAT 95% CL LAT flux upper limit plotted versus the GBM determined high-energy spectral index. The degree to which the expected flux in the LAT energy range from these bursts exceed our estimated LAT upper limits correlates strongly with the measured high-energy spectral index.

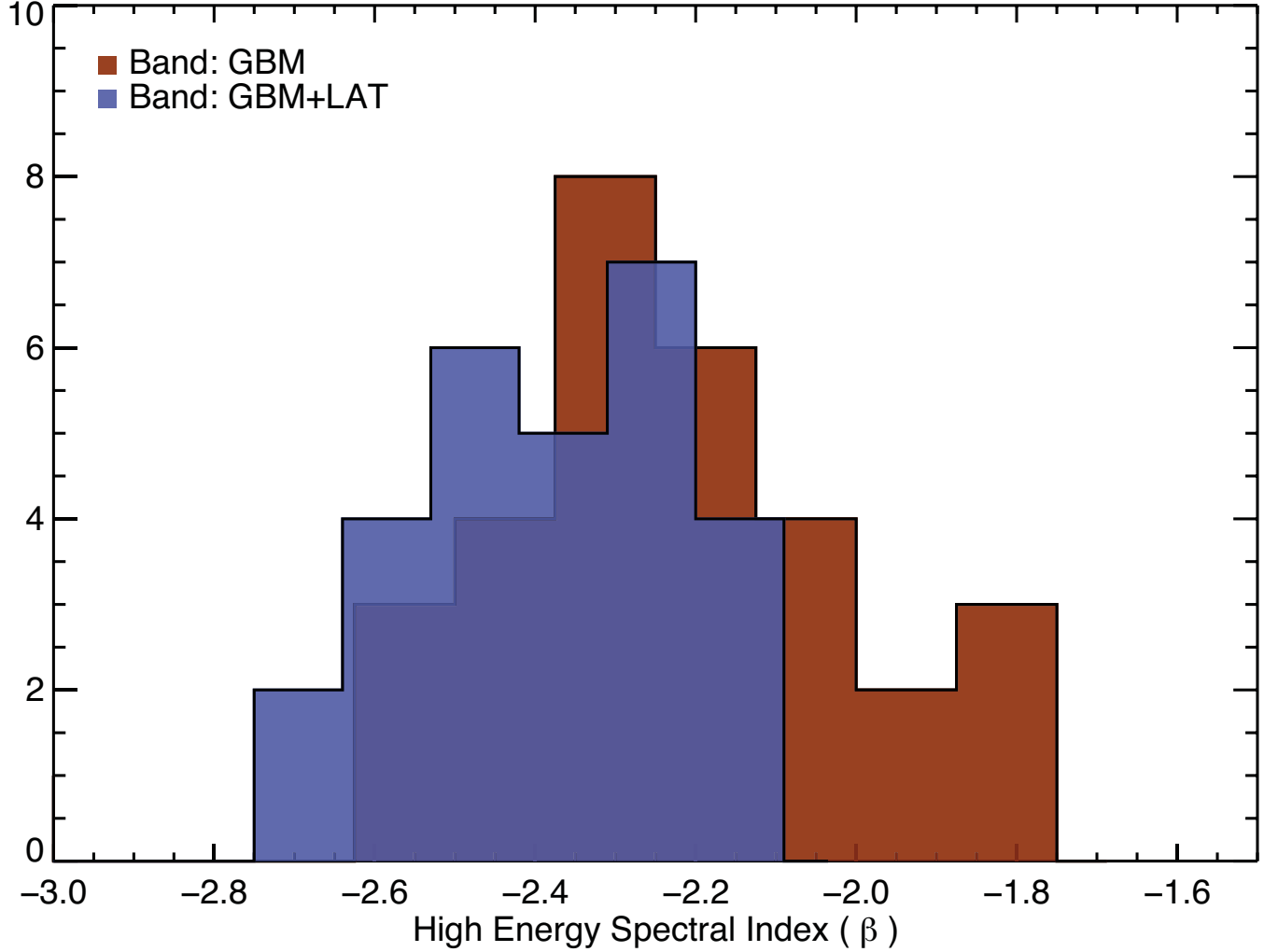


Fig. 7.— A comparison between the high-energy spectral indices measured through spectral fits to the GBM data alone and joint fits to both the GBM and LAT data. The GBM-only β distribution has a median value of $\beta = -2.2$, matching the distribution found by (Kaneko et al. 2006; Preece et al. 2000a). In contrast, the β distribution found from the joint fits indicate spectra that are considerably softer, with a median value of $\beta = -2.5$.

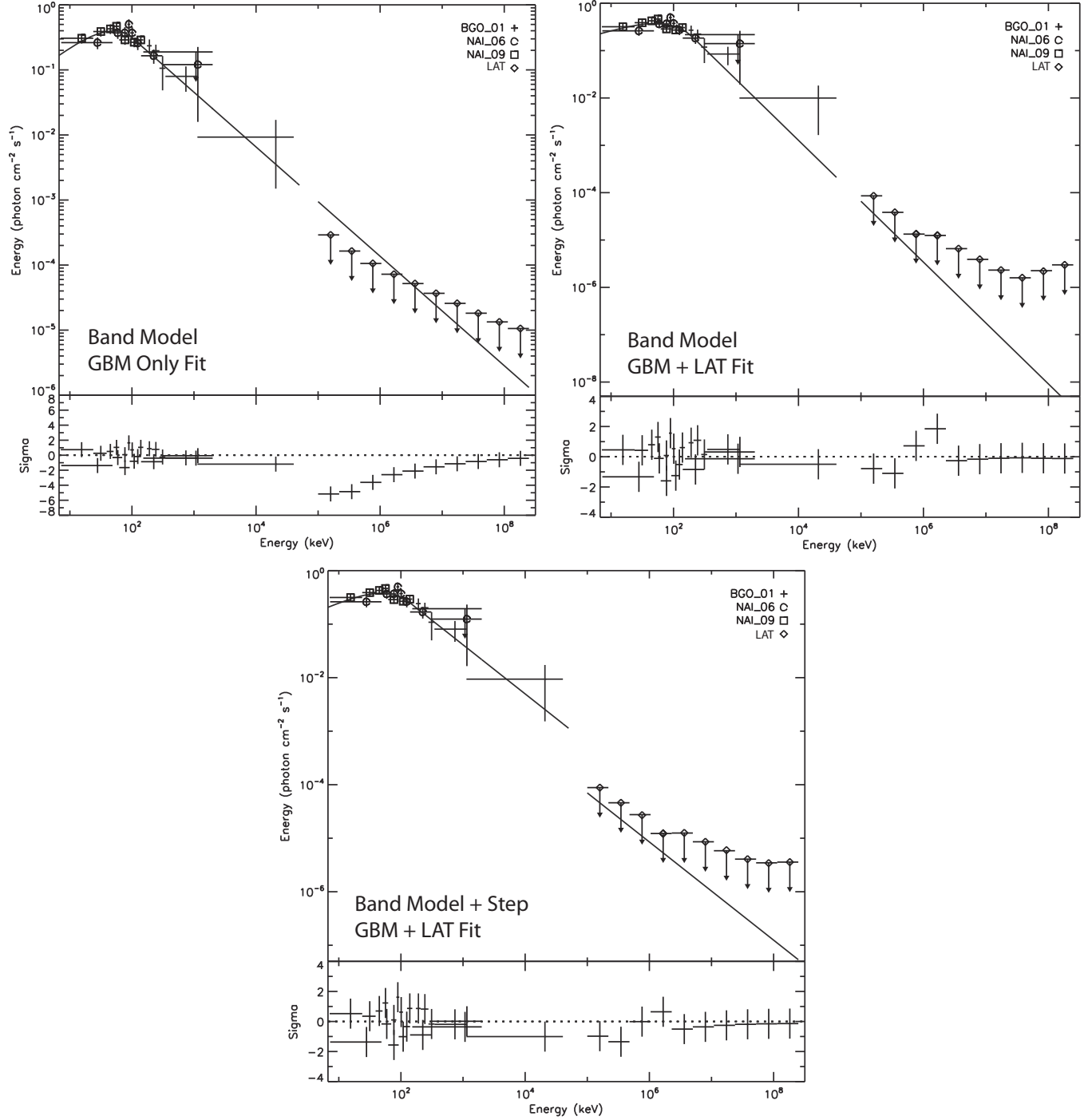


Fig. 8.— Example spectral fits showing (clockwise) a Band model fit to GBM data alone, a Band model fit to both the GBM and LAT data, and a Band model plus a step function fit to the GBM and LAT data.

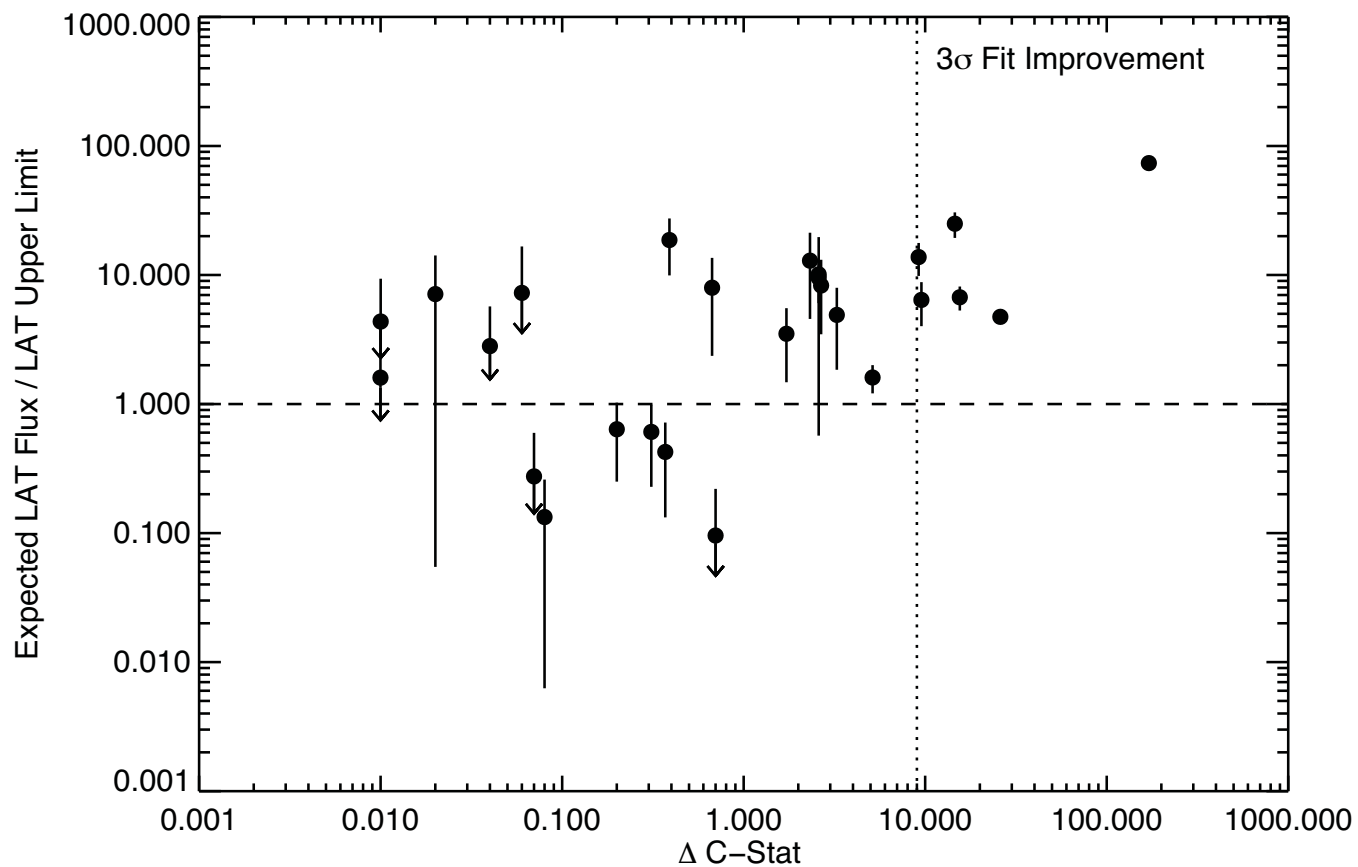


Fig. 9.— The ratio of the expected LAT flux (based on GBM-only fits) to the LAT 95% CL upper limit versus the ΔC -Stat values for our spectroscopic subsample. The long and short dashed lines represents the line of equality between the LAT upper limits and the expected LAT flux and the ΔC -Stat value representing a 3σ fit improvement respectively. The bursts for which a spectral break is statistically preferred have the most severe discrepancies between the GBM-only extrapolations and the LAT upper limits.

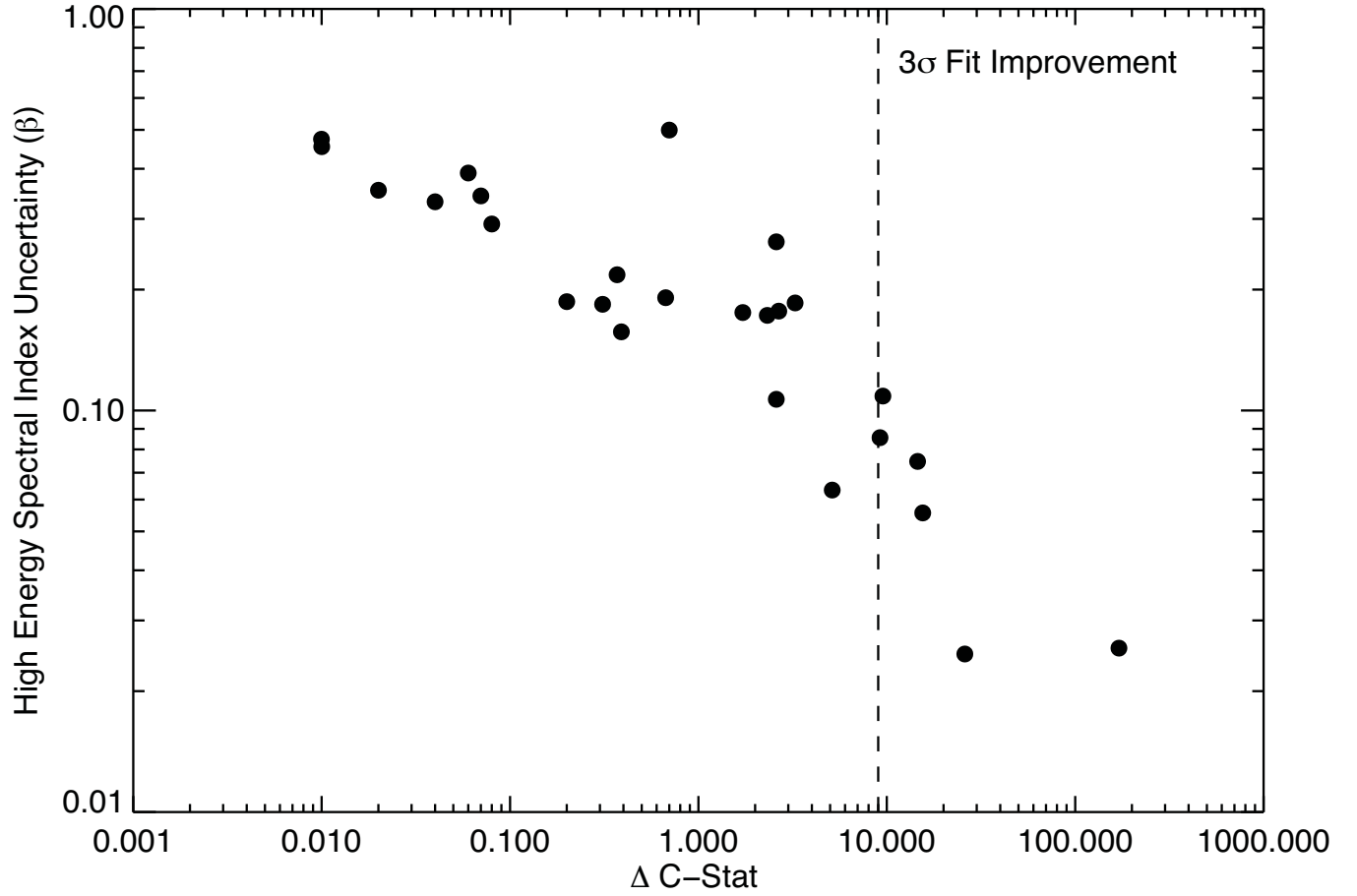


Fig. 10.— The 1σ symmetric uncertainty in the high-energy spectral index found from fits to the GBM data alone versus the Δ C-Stat values for our spectroscopic subsample. The bursts for which a spectral break is statistically preferred also have the smallest uncertainties in their GBM-only β values.

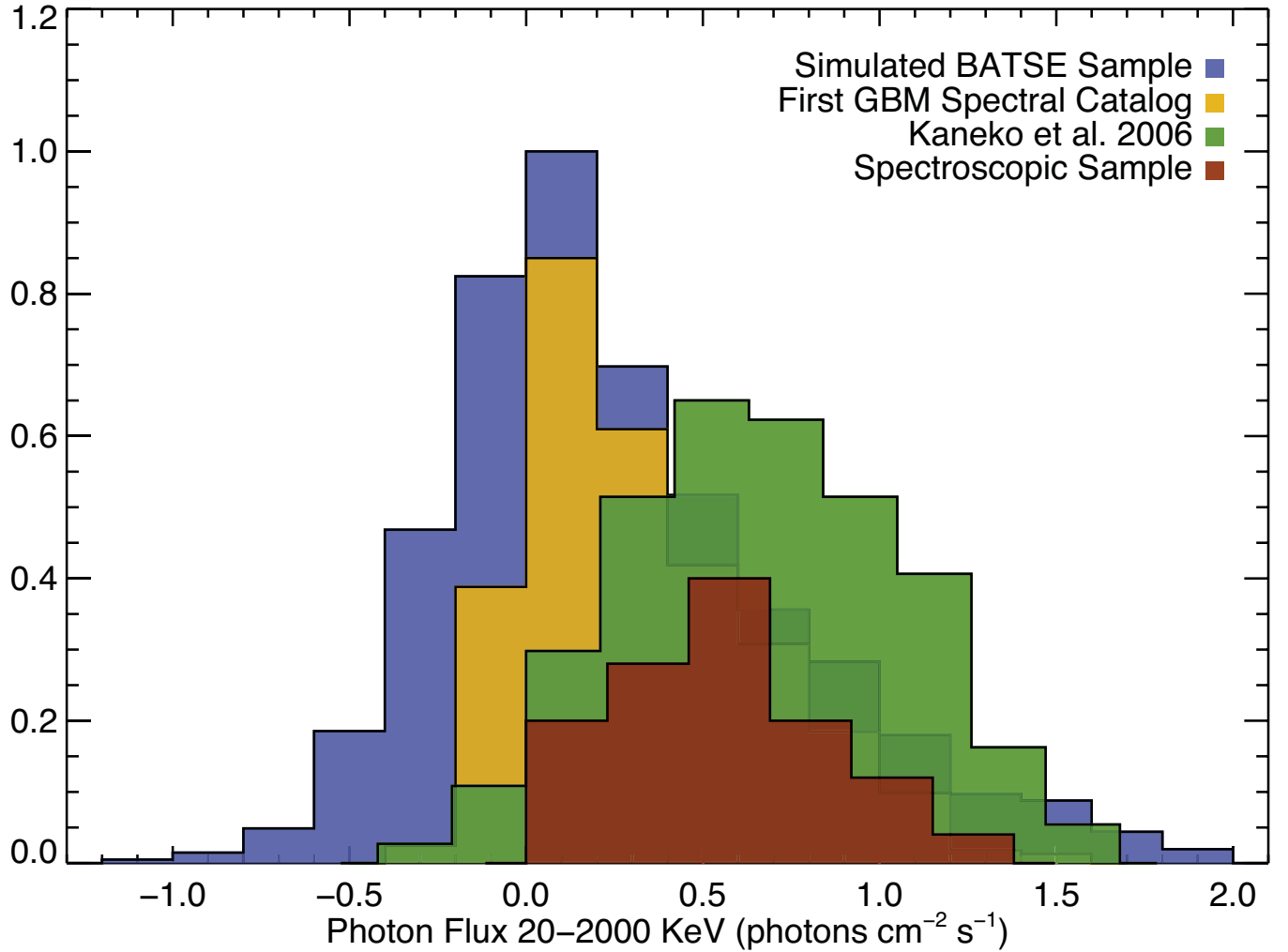


Fig. 11.— The normalized distribution of the time integrated photon flux as determined through our fits to GBM data for the spectroscopic subsample (red), the bursts in the bright BATSE catalog presented in Kaneko et al. (2006) (green), the bursts that appear in the first GBM spectral catalog (gold), and a sample of simulated BATSE bursts (blue) using the spectral parameter distributions given in Preece et al. (2000b). The resulting distributions show that our spectroscopic subsample is consistent with being drawn from the distribution of the brightest bursts detected by the GBM and BATSE.

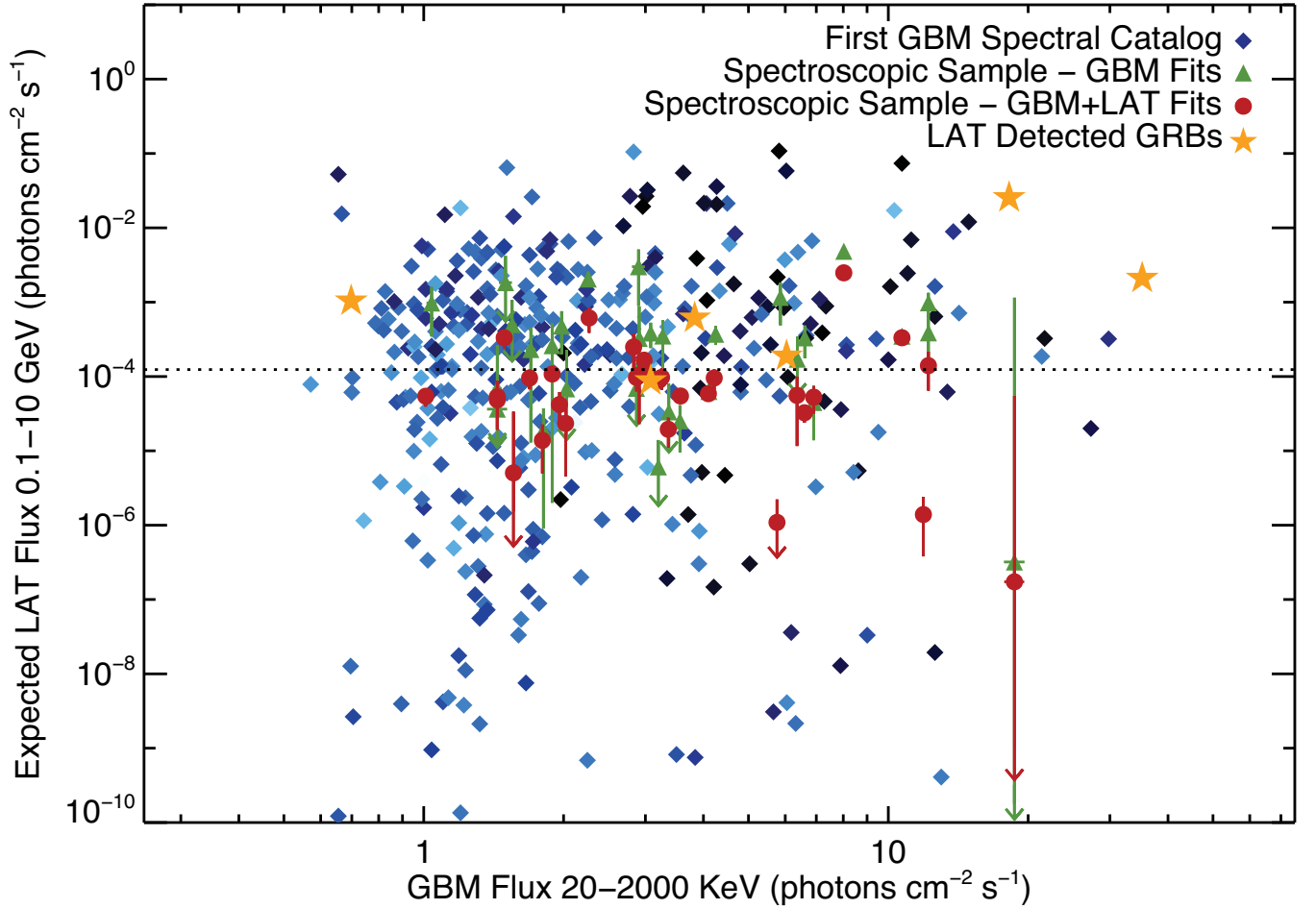


Fig. 12.— Band function model fluxes in the 0.1–10 GeV energy range versus the 0.02–2 MeV energy range for various measure and simulated data. The gold stars represent the 6 *Fermi* bursts that were detected by the LAT during the first 18 months that can be well fit by a Band function model; the green circles represent spectral fits to GBM data for the 30 bright BGO bursts in our spectroscopic subsample; the red circles represent spectral fits to GBM and LAT data for the same 30 GRBs; and the blue circles represent bursts that appear in the first GBM spectral catalog for which a Band spectral model could be fit. The color gradient in the GBM sample represents the burst’s T90 duration.

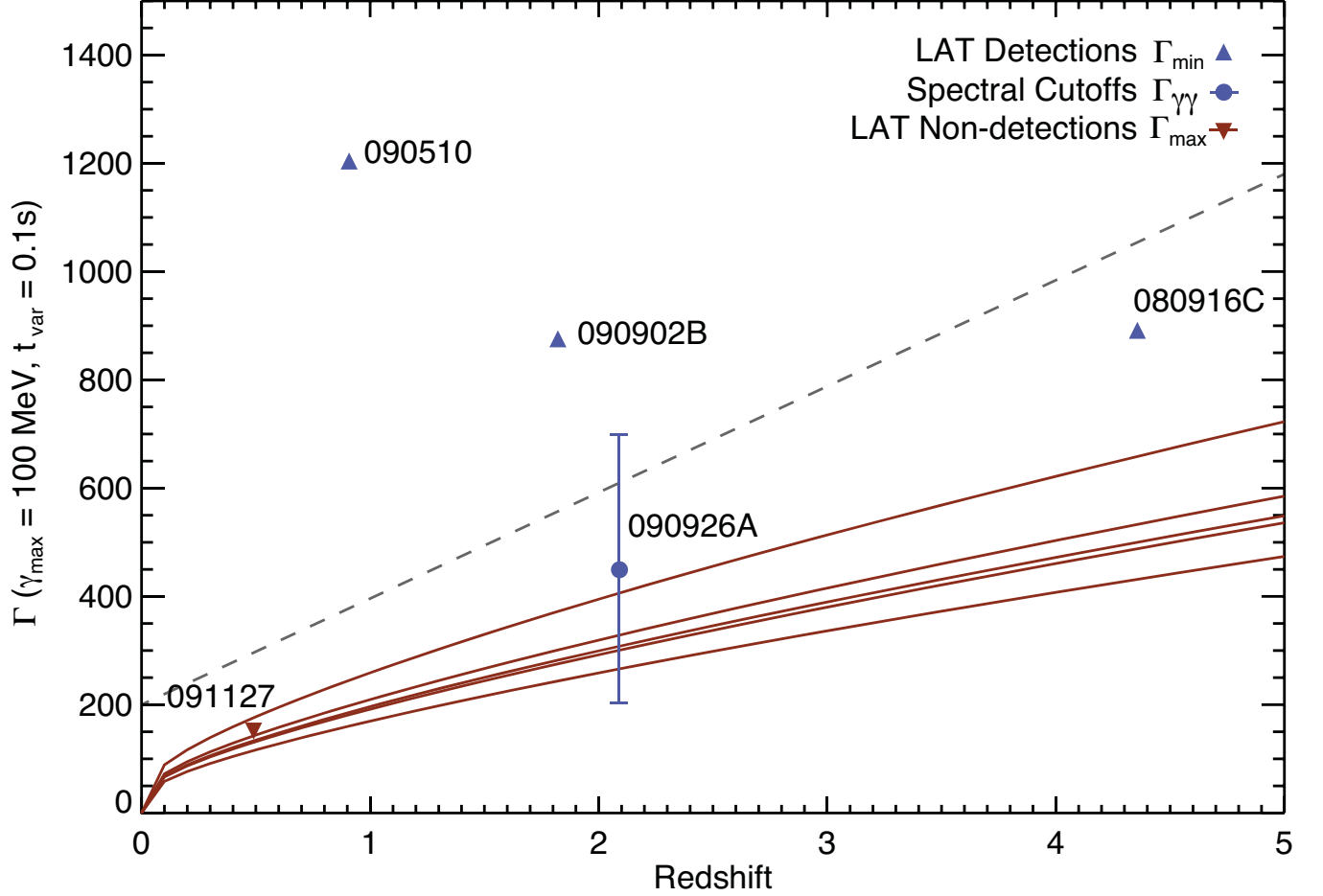


Fig. 13.— The Γ_{\max} values for the 6 GRBs in our sample with evidence for spectral breaks compared to the Γ_{\min} values for the brightest LAT-detected GRBs. The allowed range of Γ_{\max} values for $0 < z < 5$ all lie well below the Γ_{\min} values of the LAT-detected GRBs. The Γ estimate for GRB 090926A from Abdo et al. (2010) is shown as the filled blue circle. The grey dashed line demarcates the self-consistency line where the condition that $\Gamma \leq E_{\max}(1+z)/m_e c^2$ is violated. The range of Lorentz factors obtained through the use of single-zone and time-dependent models places GRB 090926A between the LAT detected and LAT dark GRBs.

Table 1. Burst Sample with Select Parameters

GRB Index	MET [†] s	RA °	Dec °	Error °	Angle [‡] °	T100 s	F _{lim,T100} ($\times 10^{-5}$ photons cm ⁻² s ⁻¹)	F _{lim,30s}	F _{lim,100s}
080804972	239584816	328.70	-53.20	0.0	56.4	22.0	7.1	5.3	1.7
080805496	239630032	322.70	47.90	5.6	13.0	28.0	-	2.3	0.8
080806896	239750976	241.80	46.70	2.9	59.6	44.0	8.4	12.4	4.0
080808565	239895232	33.60	5.40	2.6	57.9	18.0	10.5	8.1	2.3
080808772	239913104	96.70	-14.40	12.3	17.0	1.0	65.5	2.3	1.4
080810549	240066608	356.80	0.32	0.0	60.8	53.0	4.0	6.9	2.3
080816503	240581056	156.20	42.60	2.0	59.1	68.0	2.7	6.0	2.9
080824909	241307328	122.40	-2.80	1.0	18.1	10.0	7.6	4.6	1.9
080825593	241366432	232.20	-4.90	1.0	60.0	35.0	31.5	34.0	12.6
080830368	241779024	160.10	30.80	2.5	23.5	47.0	1.9	2.4	1.2
080904886	242255760	214.20	-30.30	2.1	21.8	18.0	4.2	3.3	0.9
080905499	242308736	287.70	-18.90	0.0	27.9	1.0	71.1	6.3	2.2
080906212	242370320	182.80	-6.40	1.3	34.9	3.0	60.7	3.9	1.6
080912360	242901536	25.80	-7.20	7.1	57.8	8.0	24.0	5.8	2.1
080916009	243216768	119.80	-56.60	0.0	48.8	86.0	76.7	171.8	68.6
080920268	243584752	121.60	8.90	5.4	21.0	1.0	79.9	4.9	1.2
080924766	243973360	72.80	32.50	4.4	60.1	17.0	12.0	6.2	2.1
080925775	244060560	96.10	18.20	1.2	38.0	33.0	6.0	6.6	2.7
080928628	244307104	95.10	-55.20	0.0	39.4	12.0	7.4	3.0	1.0
081003644	244740432	259.10	35.40	6.9	62.7	147.0	10.6	11.3	6.9
081006604	244996176	142.00	-67.40	8.0	16.0	144.0	1.2	3.4	0.9
081006872	245019344	172.20	-61.00	8.7	16.0	1.0	71.1	3.8	1.5
081008832	245188688	280.00	-57.40	0.0	64.2	126.0	6.2	9.6	5.9
081012549	245509824	30.20	-17.60	0.0	61.5	7.0	31.9	6.6	1.7
081024891	246576160	322.90	21.20	0.0	18.6	134.0	1.0	8.8	2.6
081101491	247232800	95.10	-0.10	0.0	29.9	1.0	71.9	3.5	1.1
081102365	247308304	225.30	22.00	8.6	61.0	147.0	2.2	6.7	2.0
081102739	247340656	331.20	53.00	0.0	50.9	41.0	3.3	4.6	2.3
081107321	247736528	51.00	17.10	3.5	52.0	3.0	60.1	4.9	2.0
081115891	248476944	190.60	63.30	15.1	53.0	1.0	131.4	4.7	2.5
081118876	248734848	54.60	-43.30	3.6	34.1	23.0	3.4	2.6	1.1
081122520	249049696	339.10	40.00	1.0	19.2	25.0	6.1	4.7	1.0

Table 1—Continued

GRB Index	MET [†] s	RA °	Dec °	Error °	Angle [‡] °	T100 s	F _{lim,T100} ($\times 10^{-5}$ photons cm ⁻² s ⁻¹)	F _{lim,30s}	F _{lim,100s}
081122614	249057808	151.40	-2.10	11.2	52.0	1.0	120.7	4.2	1.2
081126899	249428048	323.50	48.70	0.0	17.5	8.0	10.2	4.0	2.8
081204004	250041920	63.30	-62.60	4.8	57.0	3.0	77.2	5.5	2.7
081207680	250359520	112.40	70.50	1.2	60.2	101.0	8.2	11.0	5.1
081213173	250834176	12.90	-33.90	13.2	55.0	1.0	145.8	6.2	2.1
081217983	251249696	116.80	26.80	2.0	53.5	24.0	7.6	6.2	1.9
081222204	251614448	22.70	-34.10	0.0	50.0	45.0	5.9	9.2	2.7
081223419	251719440	112.50	33.20	3.8	30.0	3.0	37.6	4.5	1.1
081224887	251846272	201.70	75.10	1.0	17.9	35.0	4.7	5.1	2.3
081225257	251878160	234.10	-64.60	6.9	46.4	15.0	21.3	10.6	5.3
081226156	251955888	193.00	26.80	2.4	51.8	11.0	13.3	4.7	1.6
081226509	251986384	25.50	-47.40	0.0	22.5	1.0	75.3	2.8	1.2
081229187	252217744	172.60	56.90	8.8	44.0	1.0	86.6	2.9	0.9
081230871	252363216	207.60	-17.30	7.7	23.0	1.0	69.6	2.4	0.9
081231140	252386464	208.60	-35.80	1.0	23.3	36.0	2.1	2.5	0.8
090112332	253439840	110.90	-30.40	1.0	4.1	52.0	1.6	3.1	1.1
090113778	253564848	32.10	33.40	0.0	31.2	9.0	9.2	4.2	1.1
090117335	253872128	227.30	-41.50	4.8	63.6	3.0	117.9	9.7	3.5
090117632	253897840	121.60	-38.80	1.9	57.7	27.0	6.0	5.3	1.7
090117640	253898528	164.00	-58.20	0.0	50.9	148.0	3.7	6.8	3.4
090126227	254640384	189.20	34.10	3.6	19.0	7.0	11.0	2.5	1.3
090129880	254956032	269.00	-32.80	0.0	24.4	16.0	7.1	3.5	1.0
090131090	255060560	352.30	21.20	1.0	42.2	55.0	2.4	3.0	1.2
090202347	255255568	274.30	-2.00	2.6	57.0	15.0	12.1	6.0	2.0
090207777	255724752	252.70	34.90	3.8	46.9	14.0	9.6	5.0	1.5
090213236	256196368	330.60	-55.00	3.1	19.2	1.0	67.8	4.7	1.5
090217206	256539408	204.90	-8.40	0.0	34.5	37.0	15.4	19.1	6.9
090227310	257412352	3.30	-43.00	1.2	21.3	15.0	6.2	4.0	2.5
090228204	257489600	106.80	-24.30	1.0	16.0	1.0	68.2	2.5	0.7
090228976	257556304	357.60	36.70	3.3	21.2	5.0	16.8	2.5	1.1
090301315	257585616	352.80	9.50	5.0	54.0	4.0	43.2	4.9	1.5
090303542	257778032	223.70	-68.20	12.1	26.0	1.0	63.2	2.5	1.4

Table 1—Continued

GRB Index	MET [†] s	RA °	Dec °	Error °	Angle [‡] °	T100 s	F _{lim,T100} ($\times 10^{-5}$ photons cm ⁻² s ⁻¹)	F _{lim,30s}	F _{lim,100s}
090304216	257836256	195.90	-73.40	12.3	42.0	1.0	94.7	3.3	1.9
090305052	257908480	135.00	74.30	5.4	37.0	2.0	81.5	3.0	1.9
090306245	258011520	137.00	57.00	4.1	17.0	20.0	3.5	2.5	1.0
090308734	258226592	21.90	-54.30	4.8	50.0	1.0	111.2	8.0	2.2
090309767	258315904	174.30	-49.50	3.6	36.1	16.0	7.4	3.6	1.0
090319622	259167344	283.30	-8.90	2.6	17.9	37.0	2.4	3.0	0.9
090320045	259203920	108.30	-43.30	17.9	40.0	1.0	84.8	3.8	1.3
090320418	259236112	238.00	-46.50	12.0	61.0	1.0	194.8	17.3	5.9
090323002	259459360	190.70	17.10	0.0	57.2	144.0	6.9	14.8	9.1
090328401	259925808	90.90	-42.00	0.0	64.5	85.0	13.1	17.0	11.0
090330279	260088144	160.20	-8.20	2.1	51.4	27.0	6.3	5.7	2.1
090331681	260209216	210.50	3.10	9.3	41.0	1.0	83.9	3.1	1.4
090403314	260436768	67.10	47.20	9.7	42.1	14.0	7.6	5.0	1.8
090411838	261173200	156.00	-68.90	2.1	60.3	17.0	17.9	12.5	5.2
090413122	261284160	266.50	-9.20	5.5	50.8	12.0	23.7	7.4	2.1
090418816	261776128	262.80	-28.20	14.4	57.9	1.0	165.2	11.4	2.7
090419997	261878112	88.60	31.30	3.6	55.8	87.0	2.4	5.6	2.1
090422150	262064112	294.70	40.40	0.0	29.2	1.0	76.3	3.8	1.1
090426066	262402544	17.60	-19.20	18.1	56.0	1.0	149.8	5.2	1.8
090427644	262538816	210.00	-45.70	11.8	14.0	1.0	96.8	4.7	1.0
090429753	262721040	124.40	7.90	5.0	32.0	2.0	73.2	2.5	1.5
090510016	263607776	333.60	-26.60	0.0	13.6	1.0	1626.0	143.3	43.7
090514006	263952528	12.30	-10.90	4.6	17.0	44.0	2.3	2.3	1.2
090516137	264136640	122.20	-71.62	2.6	47.8	147.0	1.7	5.7	1.8
090516353	264155280	138.26	-11.85	0.0	19.3	85.0	1.3	2.7	1.1
090518080	264304480	119.95	0.75	0.0	36.8	1.0	78.3	3.2	1.4
090519462	264423936	119.00	-46.30	7.2	31.0	2.0	77.7	3.0	2.5
090519881	264460128	142.30	0.20	0.0	47.5	18.0	6.2	3.7	1.5
090520832	264542272	332.00	43.20	12.0	10.0	1.0	61.1	2.8	0.9
090522344	264672944	277.70	19.60	4.9	55.1	3.0	70.8	4.5	-
090524346	264845872	327.30	-66.90	1.5	62.3	55.0	4.2	8.5	2.4
090529310	265274784	231.20	32.20	7.2	39.0	147.0	1.0	3.2	1.0

Table 1—Continued

GRB Index	MET [†] s	RA °	Dec °	Error °	Angle [‡] °	T100 s	F _{lim,T100} ($\times 10^{-5}$ photons cm ⁻² s ⁻¹)	F _{lim,30s}	F _{lim,100s}
090531775	265487760	252.06	-36.05	0.0	21.9	2.0	101.3	5.7	1.8
090612619	266511056	81.03	17.71	2.2	54.1	6.0	33.6	6.1	2.6
090617208	266907600	78.89	15.65	4.2	45.0	2.0	113.5	3.5	1.0
090620400	267183392	237.35	61.15	1.0	56.0	21.0	14.4	9.9	3.6
090621185	267251200	11.02	61.94	0.0	10.9	48.0	1.8	3.3	1.0
090621417	267271248	257.49	-28.46	3.2	52.6	36.0	4.1	5.1	1.4
090623913	267486864	41.70	1.80	1.5	36.8	7.0	11.7	2.6	1.3
090625234	267601024	20.29	-6.43	3.1	13.8	13.0	5.3	2.6	0.7
090626189	267683536	169.30	-36.05	1.0	18.3	79.0	3.7	3.3	4.2
090629543	267973280	8.48	17.67	7.4	40.0	1.0	96.8	3.6	1.7
090701225	268118640	114.69	-42.07	4.2	12.0	1.0	65.5	2.5	1.7
090703329	268300448	3.30	6.90	6.6	22.0	5.0	26.1	4.1	1.4
090704783	268426016	312.97	20.43	16.5	34.5	16.0	5.3	2.8	1.2
090706283	268555648	205.07	-47.07	3.0	20.8	86.0	1.5	3.4	1.3
090708152	268717088	154.63	26.64	0.1	54.7	9.0	18.3	5.2	3.2
090709630	268844864	93.59	64.08	0.1	46.9	30.0	7.0	7.0	2.4
090711850	269036608	139.61	-64.74	1.0	12.7	46.0	1.6	2.3	1.5
090712160	269063456	70.10	22.52	0.0	33.4	150.0	1.6	5.3	1.6
090713020	269137760	284.80	-3.33	2.4	59.0	51.0	4.7	8.0	4.2
090717111	269491232	246.95	22.97	3.9	35.1	1.0	84.6	5.2	1.4
090718720	269630208	243.76	-6.68	5.9	35.7	147.0	2.4	6.6	2.2
090720710	269802176	203.00	-54.80	2.9	56.0	8.0	40.5	9.7	4.6
090722447	269952224	344.13	-62.00	31.9	1.3	154.0	1.5	4.6	1.7
090726218	270278048	238.70	32.50	6.9	52.8	8.0	-	-	-
090807832	271367872	326.90	7.23	2.6	45.0	158.0	1.6	4.8	2.0
090811696	271701728	277.05	22.22	7.5	36.7	2.0	118.8	6.4	2.1
090813174	271829440	225.80	88.60	0.0	35.3	8.0	11.1	3.9	1.4
090814368	271932576	335.90	60.30	5.9	59.0	1.0	166.6	6.2	2.3
090815946	272068896	251.30	52.90	2.4	47.5	1.0	102.0	3.5	1.6
090819607	272385280	49.10	-67.10	3.3	47.0	1.0	103.9	5.9	2.4
090820509	272463200	321.00	-4.30	10.5	44.2	12.0	8.5	3.1	1.2
090826068	272943456	140.62	-0.11	9.7	27.1	8.0	11.6	2.8	1.1

Table 1—Continued

GRB Index	MET [†] s	RA °	Dec °	Error °	Angle [‡] °	T100 s	F _{lim,T100} ($\times 10^{-5}$ photons cm ⁻² s ⁻¹)	F _{lim,30s}	F _{lim,100s}
090829672	273254848	329.20	-34.20	1.0	48.4	92.0	1.8	5.9	1.6
090829702	273257440	355.00	-9.40	3.2	42.0	24.0	5.3	5.5	2.1
090902462	273582304	264.94	27.32	0.0	50.8	30.0	265.2	265.3	84.6
090907808	274044224	81.10	20.50	3.7	32.0	1.0	-	3.1	0.9
090909854	274220992	54.18	-25.03	8.3	53.0	1.0	128.5	5.4	2.8
090917661	274895488	222.60	-19.80	7.4	37.9	3.0	40.7	3.8	1.6
090922539	275316992	13.10	74.00	1.0	20.0	146.0	1.2	3.4	1.3
090924625	275497184	50.80	-68.80	6.7	55.0	1.0	146.6	4.8	1.6
090926181	275631616	353.40	-66.32	0.0	48.1	30.0	274.7	274.8	99.9
091002685	276193568	41.00	-13.10	3.8	15.9	3.0	32.2	2.3	1.2
091003191	276237344	251.52	36.62	0.0	12.2	38.0	11.7	11.1	6.9
091010113	276835392	298.67	-22.54	0.1	55.7	15.0	18.7	9.1	3.2
091017985	277515552	204.80	-62.60	3.6	13.6	1.0	64.1	2.8	1.3
091019750	277668032	226.03	80.33	12.8	56.0	1.0	145.0	8.3	2.2
091020977	277773984	187.80	-13.40	2.2	44.9	38.0	7.4	9.5	4.2
091024380	278068000	339.25	56.89	0.0	15.5	36.0	2.0	2.5	1.0
091030613	278606592	249.00	23.54	5.6	47.9	148.0	1.8	4.5	2.6
091031500	278683232	71.70	-57.50	0.0	24.0	43.0	3.7	5.5	4.3
091103912	278978048	170.70	11.34	1.8	59.0	20.0	9.1	7.8	2.9
091107635	279299648	188.69	32.65	9.0	47.0	2.0	109.1	5.7	2.2
091109895	279494912	247.72	42.31	4.1	21.0	26.0	4.1	3.5	1.2
091115177	279951296	279.37	68.04	6.0	51.1	9.0	18.9	-	1.6
091120191	280384480	226.81	-21.79	0.5	46.0	53.0	4.2	6.9	2.4
091122163	280554848	91.28	6.02	17.7	56.0	1.0	146.0	6.8	3.4
091126389	280920000	48.72	28.26	12.6	57.0	1.0	167.7	11.1	2.6
091127976	281057152	36.60	-19.00	0.0	25.3	14.0	7.4	3.3	1.1
091202072	281411040	255.32	1.44	9.9	34.0	14.0	6.0	2.7	1.4
091207333	281865600	12.04	-48.42	1.7	36.3	146.0	1.1	3.1	1.2
091208410	281958592	29.40	16.90	0.0	55.6	16.0	25.3	17.8	4.7
091219462	282913472	294.49	71.91	5.4	36.0	1.0	78.6	3.4	0.8
091220442	282998208	167.76	3.92	1.5	60.1	23.0	12.3	9.0	2.1
091221870	283121568	55.80	23.20	0.0	53.4	34.0	5.8	6.6	1.5

Table 1—Continued

GRB Index	MET [†] s	RA °	Dec °	Error °	Angle [‡] °	T100 s	F _{lim,T100} ($\times 10^{-5}$ photons cm ⁻² s ⁻¹)	F _{lim,30s}	F _{lim,100s}
091223191	283235712	203.23	76.35	8.9	33.0	1.0	77.6	2.7	1.0
091230260	283846464	101.53	0.68	18.0	59.0	1.0	149.9	5.2	1.7
091231206	283928192	197.09	-55.95	1.5	32.2	146.0	2.3	6.4	2.4
100101028	283999200	307.32	-27.00	17.4	31.0	1.0	85.8	4.4	1.7
100101988	284082144	70.66	18.69	9.3	47.0	1.0	102.0	4.0	1.2
100107074	284521600	6.31	-21.24	6.0	53.0	111.0	1.6	5.9	1.4
100111176	284875968	247.00	15.60	0.0	32.2	8.0	11.5	3.3	0.9
100112418	284983264	242.16	-77.54	14.0	57.0	25.0	8.2	6.5	3.4
100116897	285370272	305.00	14.50	0.0	26.5	108.0	1.2	4.1	1.5
100122616	285864448	79.20	-2.71	1.3	49.2	29.0	3.9	3.8	1.1
100130729	286565376	21.19	-24.75	2.5	48.0	92.0	1.3	4.0	1.2
100131730	286651872	120.39	16.49	1.2	27.0	11.0	10.3	5.8	2.3
100201588	286725984	133.10	-37.29	4.3	45.1	147.0	1.2	4.4	1.6
100204024	286936448	50.78	-47.89	3.0	55.1	30.0	6.6	6.6	1.7
100206563	287155808	47.16	13.16	0.0	44.7	2.0	100.5	3.5	1.5
100207721	287255904	321.78	-15.78	1.0	15.0	1.0	167.9	6.6	1.8
100208386	287313344	260.25	27.53	29.3	55.0	1.0	147.8	8.1	2.3
100210101	287461504	244.38	16.08	6.1	64.0	6.0	57.0	13.7	3.4
100212550	287673120	134.27	32.22	1.4	8.0	4.0	20.5	2.7	1.3
100212588	287676448	1.82	45.96	5.0	21.6	3.0	33.3	2.3	0.8
100218194	288160736	206.64	-11.94	2.2	37.5	147.0	1.0	4.9	1.3
100221368	288435040	27.12	-17.41	8.0	60.0	12.0	-	-	-
100225115	288758720	310.30	-59.40	0.9	58.2	12.0	27.7	13.9	4.5
100225580	288798944	314.27	0.21	1.1	55.1	8.0	33.1	11.4	3.6
100225703	288809536	147.91	34.01	3.9	49.9	12.0	15.2	5.9	3.3
100227067	288927392	0.00	0.00	0.0	35.6	0.0	0.8	2.7	0.8
100228873	289083456	117.99	18.63	11.1	55.0	4.0	49.1	6.9	3.4
100301068	289100256	110.14	-15.68	7.3	42.9	1.0	125.8	3.4	1.4
100301223	289113696	201.85	19.83	4.9	56.0	9.0	18.4	7.9	2.3
100313288	290156064	172.71	-52.58	2.9	59.1	7.0	27.8	5.8	2.7
100313509	290175136	186.37	11.72	9.6	43.8	28.0	3.6	3.3	1.3
100315361	290335168	208.90	30.14	5.5	7.0	1.0	62.2	2.2	0.8

Table 1—Continued

GRB Index	MET [†] s	RA °	Dec °	Error °	Angle [‡] °	T100 s	F _{lim,T100} ($\times 10^{-5}$ photons cm ⁻² s ⁻¹)	F _{lim,30s}	F _{lim,100s}
100325246	291189280	209.14	-79.10	7.2	12.1	7.0	21.4	4.1	1.4
100325275	291191776	330.24	-26.47	0.9	9.1	8.0	18.8	6.2	2.1
100327405	291375808	334.93	-5.83	14.2	20.0	20.0	3.5	2.3	0.7
100328141	291439360	155.94	47.03	4.8	58.0	1.0	166.2	15.2	4.4
100330856	291673984	326.38	-6.97	7.7	21.0	24.0	3.0	2.4	0.8
100401297	291798464	281.85	-27.83	9.0	27.0	82.0	1.5	4.0	1.4
100414097	292904416	192.11	8.69	0.0	60.7	147.0	18.6	65.3	20.2
100417166	293169600	261.31	50.38	9.2	15.0	1.0	65.4	2.3	0.9
100420008	293415136	120.55	-5.82	2.8	58.7	25.0	10.3	8.6	2.9
100423244	293694688	119.67	5.78	1.5	40.3	13.0	7.6	6.0	2.0
100424876	293835712	7.79	43.35	2.4	53.5	27.0	7.0	6.3	1.7
100427356	294049920	89.17	-3.46	0.4	28.6	11.0	7.0	4.8	1.9
100429999	294278400	89.09	-69.96	4.0	41.0	9.0	10.6	2.9	-
100503554	294585472	147.48	3.96	1.5	61.6	135.0	2.4	8.0	3.2
100507577	294933088	2.90	-79.01	2.5	64.0	25.0	21.2	23.3	11.3
100511035	295231808	109.29	-4.65	1.0	43.6	41.0	2.6	3.6	1.1
100516014	295662016	117.32	55.14	5.3	19.0	1.0	66.7	2.5	1.1
100517132	295758592	40.63	-44.32	5.2	25.0	12.0	6.2	2.3	0.9
100519204	295937600	191.49	57.41	1.0	60.3	85.0	4.5	12.3	3.7
100527795	296679872	226.83	19.78	1.9	53.9	50.0	2.8	4.6	3.0
100528075	296704096	311.12	27.81	0.1	49.7	149.0	0.9	3.9	1.3
100604287	297327232	248.30	-73.19	3.6	52.0	13.0	13.4	5.6	1.9
100605774	297455712	273.43	-67.60	7.7	18.0	1.0	66.9	2.4	0.9
100608382	297681024	30.54	20.45	5.3	39.0	5.0	20.3	3.7	1.5
100614498	298209440	224.76	40.87	3.0	53.1	1.0	131.8	4.6	1.8
100620119	298695104	80.10	-51.68	1.5	20.1	21.0	7.0	4.8	1.5
100621529	298816928	160.86	14.72	11.4	64.0	1.0	286.7	10.7	3.0
100625891	299193760	338.26	20.29	4.4	30.8	9.0	8.8	2.5	1.0
100704149	299907296	133.64	-24.22	0.0	63.2	19.0	12.9	10.0	3.7
100715477	300886048	299.27	-54.71	9.3	42.0	14.0	7.0	3.1	1.6
100717446	301056096	304.31	19.53	9.2	59.0	1.0	165.7	9.9	2.4
100718160	301117824	121.83	-46.18	5.9	49.8	121.0	2.6	4.5	2.3

Table 1—Continued

GRB Index	MET [†] s	RA °	Dec °	Error °	Angle [‡] °	T100 s	F _{lim,T100} ($\times 10^{-5}$ photons cm ⁻² s ⁻¹)	F _{lim,30s}	F _{lim,100s}
100719311	301217312	304.87	-67.14	15.4	43.0	1.0	96.0	3.7	1.5
100719825	301261696	231.41	18.56	10.3	58.0	1.0	167.4	6.5	1.6
100722096	301457920	238.77	-15.61	1.1	32.9	13.0	6.6	2.8	1.0
100724029	301624928	124.16	74.42	1.0	51.3	100.0	6.6	11.1	6.6
100725475	301749888	292.26	76.20	4.0	19.2	1.0	66.6	2.6	1.3
100728095	301976256	88.76	-15.26	0.0	59.9	147.0	6.4	19.8	7.2
100728439	302005920	44.05	0.28	0.1	57.0	6.0	33.6	5.8	1.8
100729415	302090240	349.59	-74.86	102.8	5.6	23.0	-	-	-
100802240	302420736	2.47	47.75	0.0	64.8	150.0	8.0	16.7	14.2
100805845	302732192	112.72	-35.93	3.8	64.7	44.0	8.9	15.8	3.8
100811108	303186944	345.87	15.86	6.0	64.0	1.0	229.4	26.4	10.1
100811781	303245056	108.14	62.19	3.6	17.9	16.0	5.7	2.9	1.2
100820373	303987424	258.79	-18.51	2.1	50.0	2.0	120.9	4.8	2.2
100826957	304556320	286.43	-32.63	3.8	64.2	103.0	4.0	9.9	3.8
100829374	304765152	115.45	-3.99	4.7	61.3	80.0	3.9	7.4	3.2
100905907	305416000	262.65	13.08	4.0	61.9	12.0	32.9	12.4	4.8
100910818	305840256	238.10	-34.62	1.0	50.8	21.0	8.2	7.8	4.7
100911816	305926528	151.32	58.99	11.8	59.0	1.0	12910.0	9.4	3.4
100919884	306623552	163.24	6.02	1.8	42.1	14.0	6.9	3.3	1.4
100923844	306965728	106.12	39.60	5.3	34.0	16.0	5.6	41.1	2.2
100924165	306993504	0.67	7.00	0.0	51.0	33.0	-	-	-
100926694	307212000	43.58	-11.10	12.0	46.0	1.0	113.3	6.1	2.4
100929235	307431520	166.33	62.29	13.4	41.0	1.0	85.2	2.9	1.0
101013412	308656352	292.08	-49.64	1.6	40.0	148.0	1.9	4.4	1.6
101014175	308722304	26.94	-51.07	1.0	54.1	116.0	2.8	6.6	-
101015558	308841856	73.16	15.46	5.9	57.0	21.0	13.5	9.5	-
101017619	309019904	27.47	-26.55	4.9	35.9	20.0	4.1	3.1	1.0
101025146	309670208	240.19	-8.49	24.4	55.0	1.0	134.6	7.0	2.2
101027230	309850240	79.02	43.97	11.4	30.0	1.0	75.1	3.8	1.0
101101899	310340064	266.04	-29.00	5.4	60.2	17.0	19.2	10.1	6.7
101102840	310421408	284.68	-37.03	7.8	39.1	148.0	1.0	2.9	1.2
101107011	310781792	168.33	22.43	4.1	36.2	147.0	1.4	2.7	1.1

Table 1—Continued

GRB Index	MET [†] s	RA °	Dec °	Error °	Angle [‡] °	T100 s	F _{lim,T100} ($\times 10^{-5}$ photons cm ⁻² s ⁻¹)	F _{lim,30s}	F _{lim,100s}
101112984	311297824	100.10	9.62	5.1	46.9	70.0	1.8	4.2	1.2
101113483	311340928	29.08	0.21	2.7	46.3	147.0	0.9	3.6	1.1
101116481	311599936	32.00	-81.20	7.3	13.0	1.0	66.5	3.1	1.2
101126198	312439456	84.77	-22.55	1.0	63.5	25.0	10.5	8.9	2.9
101127093	312516832	290.31	7.89	23.2	64.9	1.0	282.1	12.4	7.6
101127102	312517664	70.95	-11.32	6.6	29.4	14.0	5.6	2.6	0.8
101128322	312623040	145.47	-35.20	5.7	7.0	2.0	62.1	3.1	0.8
101129652	312737984	157.75	-17.25	4.6	26.0	1.0	69.8	3.8	1.6
101129726	312744320	271.54	1.01	8.2	41.0	1.0	85.6	5.9	1.3
101204343	313143264	191.91	55.67	10.4	44.0	43.0	3.6	5.0	2.7
101206036	313289536	164.08	-38.11	3.5	57.5	8.0	25.2	12.8	3.2
101207536	313419104	175.75	8.72	3.7	57.3	148.0	1.3	6.2	1.6
101208203	313476768	212.40	4.04	11.7	39.2	1.0	-	-	-
101213849	313964544	260.99	-64.51	7.1	51.0	147.0	1.2	4.3	1.8
101214993	314063392	185.97	-24.27	10.0	60.0	13.0	16.2	6.7	2.1
101219686	314468896	12.23	-34.57	0.0	53.2	12.0	17.6	8.7	4.2
101220576	314545792	241.57	46.14	1.2	14.7	85.0	1.0	2.5	0.8
101220864	314570624	2.70	27.20	1.5	63.5	33.0	8.3	9.0	3.0
101224578	314891584	289.14	-55.25	4.8	49.6	47.0	2.9	3.7	1.3
101227406	315135904	240.50	-24.50	1.6	5.0	10.0	7.2	2.2	0.9
101227536	315147104	150.87	-49.44	2.6	57.7	16.0	11.5	8.3	4.0

[†]Mission elapsed time relative to January 1, 2001, 0h:0m:0s UTC

[‡]Off-axis angle with respect to the LAT boresight

Table 2. Spectral Parameters for 30 Bright GBM Detected Bursts - GBM Fits

GRB	Amplitude ($\times 10^{-2}$ photons cm^{-2} s^{-1})	α	β	E_{pk} (keV)	C-Stat
080824909	0.65 ± 0.33	-1.02 ± 0.25	-1.84 ± 0.12	113.2 ± 47.6	1.27
080906212	12.07 ± 1.58	-0.42 ± 0.09	-2.38 ± 0.13	163.9 ± 11.8	1.29
080925775	1.87 ± 0.19	-1.00 ± 0.05	-2.13 ± 0.08	136.3 ± 11.6	1.32
081122520	4.19 ± 0.44	-0.64 ± 0.07	-2.44 ± 0.23	221.2 ± 19.9	1.02
081207680	0.97 ± 0.04	-0.66 ± 0.03	-1.98 ± 0.05	417.0 ± 24.8	2.44
081223419	4.84 ± 4.20	-0.25 ± 0.46	-1.85 ± 0.14	104.4 ± 33.3	1.03
081231140	1.50 ± 0.08	-1.07 ± 0.04	-2.59 ± 0.34	251.9 ± 20.6	1.38
090129880	0.65 ± 0.10	-1.52 ± 0.09	-2.31 ± 0.53	184.7 ± 62.5	1.10
090131090	2.70 ± 0.52	-1.11 ± 0.08	-2.17 ± 0.04	55.0 ± 4.2	1.85
090514006	1.54 ± 0.56	-0.81 ± 0.19	-2.10 ± 0.19	103.9 ± 21.4	1.12
090528516	2.38 ± 0.14	-1.00 ± 0.03	-2.19 ± 0.06	163.5 ± 8.9	2.43
090612619	1.24 ± 0.15	-0.81 ± 0.10	-2.30 ± 0.41	399.1 ± 80.6	1.18
090620400	1.81 ± 0.21	-0.45 ± 0.07	-2.53 ± 0.21	157.7 ± 9.8	1.26
090829672	1.88 ± 0.04	-1.59 ± 0.01	-2.27 ± 0.11	254.4 ± 20.1	2.62
091031500	0.72 ± 0.04	-0.91 ± 0.05	-2.28 ± 0.25	474.6 ± 58.5	1.54
091109895	50.12 ± 176.00	0.78 ± 1.57	-2.28 ± 0.23	46.3 ± 13.6	1.10
091120191	2.58 ± 0.27	-1.02 ± 0.06	-2.50 ± 0.13	101.4 ± 5.8	2.30
091127976	10.01 ± 1.61	-1.28 ± 0.06	-2.22 ± 0.02	34.1 ± 1.4	1.53
091208410	1.32 ± 0.20	-1.34 ± 0.08	-2.32 ± 0.24	110.3 ± 17.3	1.30
091221870	1.20 ± 0.17	-0.76 ± 0.10	-2.09 ± 0.12	205.7 ± 26.8	1.53
100122616	6.89 ± 1.65	-0.91 ± 0.10	-2.32 ± 0.04	42.7 ± 2.3	1.49
100131730	11.80 ± 1.32	-0.57 ± 0.06	-2.21 ± 0.08	138.1 ± 8.4	1.02
100225115	0.56 ± 0.06	-0.83 ± 0.09	-2.48 ± 0.74	493.4 ± 107.0	1.37
100225580	3.71 ± 0.46	-0.76 ± 0.08	-2.11 ± 0.12	194.5 ± 21.4	1.22
100724029	3.36 ± 0.04	-0.76 ± 0.01	-2.03 ± 0.02	413.1 ± 8.9	3.19
100728095	1.33 ± 0.02	-0.86 ± 0.02	-3.03 ± 0.35	413.5 ± 13.3	15.24
101126198	3.10 ± 0.13	-1.25 ± 0.02	-2.56 ± 0.15	156.7 ± 7.5	1.62
101206036	0.49 ± 0.11	-1.13 ± 0.16	-1.84 ± 0.28	467.6 ± 324.0	1.20
101227406	3.15 ± 0.91	-0.51 ± 0.19	-2.18 ± 0.13	148.9 ± 20.9	1.48
101227536	0.48 ± 0.03	-0.73 ± 0.08	-2.26 ± 0.32	828.2 ± 172.0	1.19

Table 3. Measured and Expected Photon Fluxes in the GBM and LAT Bands

GRB	T90 (s)	Measured Flux 0.02–20 MeV (photons cm ⁻² s ⁻¹)	Expected Flux 0.1–10 GeV (×10 ⁻⁴ photons cm ⁻² s ⁻¹)	Flux Limit 0.1–10 GeV (×10 ⁻⁵ photons cm ⁻² s ⁻¹)
080824909	28.67	1.04 ± 0.04	9.75 ± 8.87	4.50
080906212	2.69	12.20 ± 0.18	3.87 ± 3.32	43.60
080925775	38.14	3.08 ± 0.03	3.85 ± 2.04	5.09
081122520	4.10	6.37 ± 0.12	1.71 ± 2.49	24.75
081207680	104.45	2.26 ± 0.02	20.50 ± 6.49	4.31
081223419	2.36	2.90 ± 0.13	30.00 ± 29.70	34.95
081231140	27.65	3.37 ± 0.04	0.34 ± 0.66	2.49
090129880	16.38	2.03 ± 0.05	0.68 ± 2.26	6.94
090131090	57.35	2.98 ± 0.03	1.64 ± 0.49	2.21
090514006	12.97	1.70 ± 0.06	2.31 ± 3.10	5.05
090528516	61.44	4.25 ± 0.03	3.71 ± 1.50	5.05
090612619	6.14	2.91 ± 0.09	3.26 ± 7.79	32.23
090620400	49.41	1.81 ± 0.03	0.19 ± 0.26	5.31
090829672	94.21	6.61 ± 0.03	3.31 ± 2.20	1.76
091031500	45.06	1.89 ± 0.03	2.60 ± 3.65	4.07
091109895	6.14	1.44 ± 0.11	0.36 ± 0.64	20.74
091120191	53.25	3.56 ± 0.04	0.25 ± 0.23	3.80
091127976	14.08	10.70 ± 0.05	3.49 ± 0.48	6.73
091208410	16.38	2.87 ± 0.06	0.69 ± 1.15	7.69
091221870	34.82	1.98 ± 0.04	4.78 ± 3.93	4.86
100122616	29.70	4.11 ± 0.04	0.63 ± 0.22	3.69
100131730	3.46	12.20 ± 0.15	9.81 ± 5.04	10.33
100225115	18.99	1.44 ± 0.05	0.69 ± 2.73	7.16
100225580	5.12	5.86 ± 0.10	11.60 ± 9.48	25.36
100724029	100.35	8.02 ± 0.03	48.40 ± 5.20	13.52
100728095	147.46	3.20 ± 0.02	0.06 ± 0.11	3.81
101126198	25.60	6.91 ± 0.05	0.45 ± 0.44	10.43
101206036	17.92	1.44 ± 0.07	23.70 ± 39.70	13.89
101227406	10.50	3.27 ± 0.10	3.51 ± 3.10	6.23
101227536	18.82	1.55 ± 0.05	5.00 ± 8.10	13.32

Table 4. Spectral Parameters for 30 Bright GBM Detected Bursts - GBM & LAT Fits

GRB	Amplitude ($\times 10^{-2}$ photons $\text{cm}^{-2} \text{s}^{-1}$)	α	β	E_{pk} (keV)	Cash	DOF	$\Delta\beta$	$\Delta\text{C-Stat}$
080824909	0.53 ± 0.12	-1.11 ± 0.13	-2.41 ± 0.15	151.2 ± 31.3	475.73	378	-0.56 ± 0.15	2.32
080906212	10.79 ± 1.10	-0.48 ± 0.07	-2.55 ± 0.12	176.4 ± 10.1	639.11	504	-0.17 ± 0.12	0.20
080925775	1.70 ± 0.12	-1.05 ± 0.04	-2.42 ± 0.09	154.0 ± 9.4	500.77	380	-0.30 ± 0.09	9.53
081122520	3.99 ± 0.35	-0.67 ± 0.07	-2.64 ± 0.19	232.7 ± 17.0	501.82	502	-0.20 ± 0.19	0.04
081207680	0.87 ± 0.02	-0.73 ± 0.02	-2.70 ± 0.12	528.2 ± 24.3	952.43	385	-0.72 ± 0.12	14.57
081223419	2.57 ± 1.02	-0.57 ± 0.25	-2.23 ± 0.15	149.6 ± 32.0	399.95	380	-0.37 ± 0.15	0.67
081231140	1.46 ± 0.07	-1.08 ± 0.03	-3.46 ± 0.71	265.7 ± 16.0	509.18	378	-0.88 ± 0.71	0.01
090129880	0.61 ± 0.07	-1.55 ± 0.07	-4.16 ± 36.00	219.9 ± 56.2	406.74	379	-1.85 ± 36.00	0.00
090131090	1.62 ± 0.16	-1.33 ± 0.05	-2.42 ± 0.09	73.8 ± 4.6	696.42	374	-0.25 ± 0.09	15.51
090514006	1.49 ± 0.41	-0.82 ± 0.15	-2.30 ± 0.10	109.1 ± 15.1	424.25	380	-0.19 ± 0.10	2.59
090528516	2.14 ± 0.09	-1.06 ± 0.03	-2.49 ± 0.11	187.2 ± 8.6	1216.40	504	-0.30 ± 0.11	9.20
090612619	1.18 ± 0.10	-0.84 ± 0.08	-3.41 ± 0.66	444.0 ± 65.5	436.14	379	-1.11 ± 0.66	0.00
090620400	1.77 ± 0.18	-0.47 ± 0.07	-2.60 ± 0.14	160.0 ± 8.6	469.50	377	-0.07 ± 0.14	0.08
090829672	1.83 ± 0.03	-1.60 ± 0.01	-3.07 ± 0.48	287.0 ± 17.3	972.98	379	-0.80 ± 0.48	0.39
091031500	0.70 ± 0.03	-0.92 ± 0.04	-2.63 ± 0.09	501.1 ± 50.2	567.74	378	-0.35 ± 0.09	0.02
091109895	54.26 ± 190.00	0.81 ± 1.58	-2.24 ± 0.11	45.6 ± 12.3	272.81	255	0.04 ± 0.11	-0.04
091120191	2.53 ± 0.24	-1.03 ± 0.05	-2.56 ± 0.11	103.1 ± 5.1	589.17	262	-0.06 ± 0.11	0.31
091127976	8.55 ± 1.16	-1.34 ± 0.06	-2.26 ± 0.02	36.4 ± 1.4	774.38	495	-0.04 ± 0.02	25.95
091208410	1.35 ± 0.20	-1.33 ± 0.07	-2.28 ± 0.07	107.4 ± 13.9	480.39	376	0.04 ± 0.07	0.07
091221870	1.06 ± 0.10	-0.84 ± 0.07	-2.48 ± 0.11	241.0 ± 22.8	571.15	379	-0.40 ± 0.11	2.67
100122616	6.01 ± 1.28	-0.96 ± 0.09	-2.38 ± 0.05	44.6 ± 2.3	557.59	379	-0.06 ± 0.05	5.13
100131730	8.07 ± 0.48	-0.78 ± 0.04	-3.32 ± 0.20	183.8 ± 7.3	399.27	382	-1.11 ± 0.20	2.59
100225115	0.56 ± 0.05	-0.83 ± 0.09	-2.54 ± 0.17	496.8 ± 94.8	506.20	379	-0.06 ± 0.17	-0.02
100225580	3.02 ± 0.21	-0.88 ± 0.05	-3.25 ± 0.24	248.8 ± 17.7	619.61	509	-1.14 ± 0.24	1.72

Table 4—Continued

GRB	Amplitude ($\times 10^{-2}$ photons $\text{cm}^{-2} \text{s}^{-1}$)	α	β	E_{pk} (keV)	Cash	DOF	$\Delta\beta$	$\Delta\text{C-Stat}$
100724029	3.08 ± 0.03	-0.82 ± 0.01	-2.51 ± 0.03	502.1 ± 8.6	1435.30	378	-0.48 ± 0.03	170.70
100728095	1.33 ± 0.02	-0.86 ± 0.02	-2.84 ± 0.12	410.8 ± 12.4	5633.20	379	0.19 ± 0.12	0.70
101126198	3.08 ± 0.12	-1.26 ± 0.02	-2.62 ± 0.16	158.4 ± 7.2	603.71	379	-0.06 ± 0.16	0.37
101206036	0.49 ± 0.07	-1.12 ± 0.12	-2.45 ± 0.27	514.9 ± 209.0	445.33	378	-0.62 ± 0.27	0.06
101227406	2.18 ± 0.38	-0.74 ± 0.13	-2.53 ± 0.20	188.7 ± 21.3	549.62	378	-0.35 ± 0.20	3.26
101227536	0.47 ± 0.03	-0.75 ± 0.07	-3.65 ± 0.86	930.3 ± 164.0	440.63	378	-1.39 ± 0.86	0.01

REFERENCES

623

624 Abdo, A. A., et al. 2009a, *ApJ*, 706, L138

625 —. 2009b, *ApJ*, 706, L138

626 —. 2009c, *ApJ*, 707, 580

627 —. 2009d, *Science*, 323, 1688

628 —. 2010, *ApJ*, submitted

629 Ackermann, M., et al. 2010a, *ApJ*, 716, 1178

630 —. 2010b, *ApJ*, 716, 1178

631 —. 2011a, *ApJ*, 729, 114

632 —. 2011b, *ApJ*, 729, 114

633 Amsler, C., et al. 2008, *Phys. Lett.*, B667, 1

634 Atwood, W. B., et al. 2009, *ApJ*, 697, 1071

635 Band, D., et al. 1993, *ApJ*, 413, 281

636 Band, D. L., et al. 2009, *ApJ*, 701, 1673

637 Baring, M. G. 2006, *ApJ*, 650, 1004

638 Bissaldi, E., et al. 2011, *ApJ*, 733, 97

639 Brown, R. W., Mikaelian, K. O., & Gould, R. J. 1973, *Astrophys. Lett.*, 14, 203

640 Cash, W. 1976, *A&A*, 52, 307

641 Castor, J. 1995, private communication

642 Cucchiara, A., Fox, D., Levan, A., & Tanvir, N. 2009, *GRB Coordinates Network*, 10202, 1

643 Del Monte, E., et al. 2011, *A&A*, 535, A120

644 Fan, Y., & Piran, T. 2008, *Frontiers of Physics in China*, 3, 306

645 Gehrels, N., et al. 2004, *ApJ*, 611, 1005

- 646 González, M. M., Dingus, B. L., Kaneko, Y., Preece, R. D., Dermer, C. D., & Briggs, M. S.
647 2003, *Nature*, 424, 749
- 648 Gould, R. J., & Schröder, G. P. 1967, *Physical Review*, 155, 1408
- 649 Granot, J., Cohen-Tanugi, J., & do Couto e Silva, E. 2008, *ApJ*, 677, 92
- 650 Guiriec, S., et al. 2011a, *ApJ*, 727, L33+
- 651 —. 2011b, *ApJ*, 727, L33
- 652 Hascoët, R., Daigne, F., Mochkovitch, R., & Vennin, V. 2011, *ArXiv e-prints*
- 653 Helene, O. 1983, *Nuclear Instruments and Methods in Physics Research*, 212, 319
- 654 Hurley, K., et al. 1994, *Nature*, 372, 652
- 655 Jackson, B., et al. 2005, *Signal Processing Letters, IEEE*, 12, 105
- 656 Kaneko, Y., Preece, R. D., Briggs, M. S., Paciasas, W. S., Meegan, C. A., & Band, D. L.
657 2006, *ApJS*, 166, 298
- 658 Kouveliotou, C., et al. 1994, *ApJ*, 422, L59
- 659 Kraft, R. P., Burrows, D. N., & Nousek, J. A. 1991, *ApJ*, 374, 344
- 660 Lithwick, Y., & Sari, R. 2001, *ApJ*, 555, 540
- 661 Mattox, J. R., et al. 1996, *ApJ*, 461, 396
- 662 McBreen, S., et al. 2010, *A&A*, 516, A71
- 663 Meegan, C., et al. 2009a, *ApJ*, 702, 791
- 664 —. 2009b, *ApJ*, 702, 791
- 665 Preece, R. D., Briggs, M. S., Mallozzi, R. S., Pendleton, G. N., Paciasas, W. S., & Band,
666 D. L. 2000a, *ApJS*, 126, 19
- 667 —. 2000b, *ApJS*, 126, 19
- 668 Razzaque, S., Mészáros, P., & Zhang, B. 2004, *ApJ*, 613, 1072
- 669 Sommer, M., et al. 1994, *ApJ*, 422, L63
- 670 Walker, K. C., Schaefer, B. E., & Fenimore, E. E. 2000, *ApJ*, 537, 264

